Experimental and numerical investigation on the performance of three-legged CFST latticed columns under lateral cyclic loadings

You-Fu Yang[a,*], Min Liu[a], Feng Fu[b]

[a] *State Key Laboratory of Coastal and Offshore Engineering, Dalian University of Technology, Dalian, 116024, China*

[b] *Department of Civil Engineering, School of Mathematics, Computer Science & Engineering, City University London, Northampton Square, London, UK*

Abstract:

To evaluate the cyclic performance of composite latticed columns, experiments and numerical modelling of three-legged concrete filled steel tube (CFST) latticed columns under constant axial compressive force and lateral cyclic loadings were conducted. Experiments of eight specimens, including 6 CFST latticed columns and 2 steel latticed columns, were carried out with various axial compression ratio and diameter-to-thickness ratio of the tube section in the limb. The failure pattern, hysteretic behaviour, bearing capacity, initial stiffness and accumulated energy dissipation of the specimens were investigated. The experimental results reveal that, under cyclic loadings, CFST latticed columns have better performance than the corresponding steel latticed columns; however, three-legged CFST latticed specimens show different behaviour in two loading directions owing to the different capacity of the CFST members under tension and compression. A finite element analysis (FEA) model was developed to simulate the performance of three-legged CFST latticed columns under lateral cyclic loadings, and the feasibility of the FEA model was verified by the comparison against test results.

Key Words: concrete filled steel tube (CFST); latticed columns; three-legged; lateral cyclic loadings; experiments; finite element analysis (FEA).

*Corresponding author. Tel.: 86-411-8470 8510; Fax: 86-411-8467 4141.
E–mail address: youfuyang@163.com (Dr. You-Fu Yang).

1. Introduction

Single concrete filled steel tube (CFST) members are widely used in building structures and bridges owing to their high strength, high ductility and toughness, fast track construction and low cost features, which is due to the composite action between steel tube and its core concrete (Han et al. 2014)[1]. However, in engineering practice, tensile stresses can be observed in the concrete core of CFST when the members undertake a load with a larger eccentricity ratio or when it is used as a column with a larger slenderness ratio, which results in a weaker confinement of steel tube to its core concrete, and therefore, the advantage of CFST cannot be fully explored. To tackle this problem, the CFST latticed members are designed as it is shown in Fig. 1. Through a rational combination of limbs and lacings, CFST latticed members have relative large moment of inertia owing to their main load-bearing limbs being placed away from the centroid axis, which in turn, resulting a lighter weight, a better stability and a larger flexural rigidity in comparison to the single CFST members. Currently, CFST latticed members are mainly used as bridge piers, bridge towers, key arch rib element in the arch bridge, transmission tower or wind power tower, supporting pillar in high-rise buildings, bracing system of large-span structures, etc. (Kawano and Sakino 2003; Ou et al. 2011; Huang 2015)[2-4], and in these engineering fields the anti-seismic capacity of CFST latticed members is crucial to guarantee the safety of structures located at the earthquake fortification zone.

Compared with the conventional four-legged CFST latticed member, three-legged CFST latticed member is more stable due to its triangle shape and is more economical as one limb and a column of lacings are removed. Moreover, three-legged CFST latticed member has obvious directionality and is more applicable for structures with supporting on one side. As a result, three-legged CFST latticed members are more suitable to be used as the edge or corner columns for a factory building, arch rib of arch bridge and truss beams of a bridge or building.

The earliest experimental research on the structural behaviour of two-legged CFST latticed columns [Fig. 1(a)] under lateral cyclic loadings was conducted by Kawano et al. (1996)[5], and it

was shown that the rigidity and strength of connections between CFST limbs and tube lacings were improved compared to the corresponding steel latticed columns. After that, the scholars began to pay close attention to the seismic behaviour of four-legged CFST latticed members with various lacing arrangements, and more experimental and theoretical investigations had been carried out, as summarized in Table 1, where H is the height of the specimen, D_s and T_s are the tube external diameter and thickness of the limbs respectively, d_w and t_w are the tube external diameter and thickness of the lacings respectively, f_{ys} and f_{yw} are the steel yield strength of the limbs and lacings respectively, f_{cu} is the cube compressive strength of core concrete in the limbs, λ^* is the conversion slenderness ratio of the specimen determined according to a specification related to design of CFST structures (DBJ13-51 2003)[10], and n is the axial compression ratio. Both pseudo-static (Kawano et al. 1996; Deng 2012; Luo 2013; Chen et al. 2014; Huang 2015; Yuan et al. 2016)[4-9] and pseudo-dynamic (Deng 2012)[6] testing methods were considered in the experimental investigation, and numerical simulations were further carried out by using the software packages ABAQUS (Deng 2012; Luo 2013)[6,7] and OpenSees (Huang 2015; Yuan et al. 2016)[4,9]. It can be concluded from the literature review that there is little research on the performance of three-legged CFST latticed columns subjected to cyclic loadings, which indicates the study of this subject is timely.

The objective of this paper is to present an experimental and numerical investigation on the behaviour of three-legged CFST latticed columns subjected to constant axial compressive force and lateral cyclic loadings. The effect of axial compression ratio and diameter-to-thickness ratio of the tube section in the limb on the performance of this type of columns under lateral cyclic loadings was investigated through the test. The comparison between CFST latticed specimens and the steel counterparts was also carried out. Apart from that, a finite element analysis (FEA) model was constructed to predict the responses of three-legged CFST latticed columns under lateral cyclic loadings, and the comparison between the numerical and experimental results was made to assess the accuracy of the FEA model.

2. Experimental program

2.1. Specimen preparation

Eight three-legged specimens, including 6 CFST latticed columns and 2 steel latticed columns, were prepared. The schematic diagram of CFST and steel latticed specimens is demonstrated in Fig. 2, and the detailed setting up of the tested specimens is given in Table 2, where l_w is the length between internodes, h_0 is the centroid distance of two limbs, N_0 is the constant axial compressive force applied to the latticed columns, P_{ue+} and P_{ue-} are the measured bearing capacity in push and pull loading direction respectively (see Fig. 3), P_{uc+} and P_{uc-} are the predicted bearing capacity in push and pull loading direction respectively, and S_i is the initial stiffness of the tested specimens.

An important goal during the design of the experimental program is to evaluate the influence of the following parameters on the cyclic performance of the tested specimens:

● Axial compression ratio, n : from 0.05 to 0.52;

● Diameter-to-thickness ratio of the tube section in the limb, D_s / T_s : 24.9 and 51.5; and

● Type of the limb: CFST and steel tube.

The conversion slenderness ratio (λ^*) of CFST and steel latticed specimens, which represents the effect of the shear deformation of lacings on the stability strength, was calculated according to the formulae in DBJ 13-51 (2003)[10] and GB 50017 (2003)[11], respectively. The detailed formulae for λ^* are as follows:

$$\lambda^* = \begin{cases} \sqrt{\lambda_y^2 + 200 A_s / A_w} & \text{(CFST latticed specimen)} \\ \sqrt{\lambda_y^2 + 42 A / (A_l \cdot \cos^2 \theta)} & \text{(Steel latticed specimen)} \end{cases} \tag{1}$$

where, λ_y is the slenderness ratio of the specimen about the bending neutral axis (Y-Y axis in Fig. 2); A_s and A_w are the steel tube area of single limb and lacing, respectively; A and A_l are the

total area of all limbs and diagonal lacings within the cross-section respectively, and θ is the angle between the plane with diagonal lacings and solid axis (X-X axis in Fig. 2).

The axial compression ratio (n) of the tested specimens is defined as:

$$n = \frac{N_0}{\varphi \cdot N_u} \tag{2}$$

where, φ is the stability factor related to the conversion slenderness ratio (λ^*), and N_u is the sectional bearing capacity under concentric compression determined using the formulae in DBJ 13-51 (2003)[10] and GB 50017 (2003)[11] for CFST and steel latticed columns, respectively.

Two types of cold-formed circular hollow sections (CHS) were chosen for the tube in the limbs and tube lacings. The mechanical properties of steel tube in the limbs were obtained by tensile tests of three coupons randomly cut from the CHS members. In the meantime, compressive tests on three stub specimens with length-to-diameter of 3.0 were performed to acquire the properties of the tube lacings. From the tests, the average yield strength, tensile strength, elastic modulus, Poisson's ratio and elongation after fracture were received, as presented in Table 3.

Self-consolidating concrete (SCC) was prepared to fill the tube in the limbs of CFST latticed specimens. Table 4 shows the mix proportions and properties of the SCC. To measure the compressive strength and elastic modulus of the SCC, several cubes with a length of 150 mm and prisms of size 150 mm×150 mm×300 mm were cast and cured in conditions similar to the CFST latticed specimens. The curing conditions for the SCC standard specimens were maintained constant at 20 ℃±2 ℃ and 95% relative humidity. The measured cube compressive strength (f_{cu}) of the SCC at 28 days and during the loading tests was equal to 50.1 MPa and 55.9 MPa respectively, and the mean elastic modulus of the SCC was 33,600 N/mm².

2.2. Test set-up and instruments

Tests of three-legged latticed specimens were carried out under combined constant axial compressive force and lateral cyclic loadings, and the schematic view and real scenario of the test set-up and instruments are demonstrated in Fig. 3. A 2000 kN actuator was used to exert the

constant axial compressive force (N_0) during the tests, and the maximum deviation of N_0 was within 10%, as shown in Fig. 4. The loadings were applied by imposing lateral cyclic displacements at the top of the specimens via an actuator with 500 kN capacity. The bottom endplate of the specimens was connected to a baseplate using 20 high-strength bolts, and the baseplate was further fixed to the ground through 2 reaction beams and 4 anchor rods. A total of thirteen displacement transducers (DTs) were used in each test, in which ten DTs acted on limbs C1 and C2 (DT_{1i} and DT_{2i}, i=1-5) were used to obtain the lateral displacements at the connection between the limb and lacings, two DTs located at the ends of the top endplate (DT_{t1} and DT_{t2}) were used to acquire the possible relative torsion angles according to the lateral displacement differences over the width of the endplate, and one DT located at the middle of the top endplate (DT_0) was used to monitor the lateral displacements at the top of specimen. Moreover, six strain gauges were mounted at the exterior surface of the selected position of limbs C1 and C3 and one lower lacing to measure the development of the strains in both longitudinal and transverse directions, and their detailed positions are shown in Fig 3.

As is known, cyclic seismic testing of single CFST columns following the procedures in the ATC24 (1992)[12] had been reported by the researchers (Varma et al. 2004; Zhou and Xu 2016)[13,14], and the precise bearing capacity of the member under constant axial compression and lateral loading, which determines the loading histories in the force control stage and the yield displacement of the specimens, should be known in advance. However, for the three-legged CFST latticed members, there is no accurate method available to date for assessing the bearing capacity while subjected to compression and bending, and an inaccurate value may result in the premature failure of the specimens or the inaccurate displacement reading when yielding starts. As a result, the loading histories with the displacement control were adopted to ensure accurate data acquisition in the test of three-legged CFST latticed specimens under combined constant axial compressive force and lateral cyclic loadings. The history of the lateral displacements at the top of the column (Δ_{top}) was divided into increments and the peak displacement of each step j was given as δ_j,

$$\delta_j = \begin{cases} j \cdot \Delta_0 / 4 & (1 \le j < 4) \\ (j/2-1) \cdot \Delta_0 & (4 \le j < 6) \\ (j-4) \cdot \Delta_0 & (j \ge 6) \end{cases} \tag{3}$$

where, Δ_0 is equal to 10 mm. The load increment was controlled by displacement through setting the loading frequency (f_L) to be 0.01 Hz, 0.008 Hz, 0.005 Hz, 0.004 Hz and 0.002 Hz while $\delta_j \le 20$ mm, $\delta_j = 30$ mm, $\delta_j = 40$ and 50 mm, $\delta_j = 60$ mm and $\delta_j \ge 70$ mm, respectively. One cycle was applied at each displacement level when j was less than 4 and after that three cycles were applied at each displacement level. The curve of the loading protocol is given in Fig. 5, where n_c is the number of cycles. The testing was ceased when the lateral load resistance decreased below 50% of the maximum bearing capacity of the specimen in either loading direction or the severe deterioration to the limbs, lacings or the connection between them were observed.

3. Test results and discussion

3.1. Overall observations and failure pattern

The structural responses of the specimens under constant axial compressive force and lateral cyclic loadings were initially dominated by a combination of local deformation and global displacement, and the specimens demonstrated the conventional cantilever beam-column failure mechanism due to both compression and bending.

To evaluate the torsion effect of the specimens, relative torsion angle of the top endplate (θ_{rt}) of the specimens is defined as:

$$\theta_{rt} = \left| \frac{\Delta_{DT_{t1}} - \Delta_{DT_{t2}}}{D_e} \right| \tag{4}$$

where, $\Delta_{DT_{t1}}$ and $\Delta_{DT_{t2}}$ are the measured lateral displacements using the displacement transduces DT_{t1} and DT_{t2} (see Fig. 3), respectively, and D_e is the width of the endplate.

Variation of θ_{rt} with Δ_{top}/H is shown in Fig. 6. It can be seen that, for any given specimen, a symmetric distribution of θ_{rt} in two loading directions can be observed, which increases in pace

with increase of Δ_{top}/H. Overall, the maximum θ_{rt} is less than 0.8%, and during the cyclic loading process of specimens the torsion effect is not obvious, i.e. three-legged CFST latticed specimens have good out-of-plane stability and no further out-of-plane constraint is needed in the tests. It is believed that the lateral displacements along the height of the specimens generally belongs to the in-plane deformation.

It was found that the lateral displacements at limbs C1 and C2 were kept almost same except for the last few loading steps, and this is due to the serious damage of both limbs and lacings. The lateral displacements at measurement point i (Δ_i) of the typical specimens during the first cycle of each step are shown in Fig. 7, where y is the distance from the bottom end of specimens, and p ($=P/P_{\text{ue+}}$ or $P/P_{\text{ue-}}$, in which P is the applied lateral load by the actuator) is the load level and the minus values represent the descending stage after peak load. It can be seen that, in general, there is an approximate linear relationship between Δ_i/Δ_0 and y/H regardless of the type of the limb. Under the same δ_i, steel latticed specimens generally have similar p values in two loading directions; however, for CFST latticed specimens the value of p in pull loading direction is evidently different from those in push loading direction. This means that the effect of the asymmetry caused by the triangular layout of the limbs in the CFST latticed specimens is severer than that of the steel counterparts, which is due to the fact that the difference in mechanical property under tension and compression of steel tube is less than that of CFST under the same dimensions and material properties. Furthermore, before achieving the peak load, p increases with increase of D_s/T_s under the same δ_i irrespective of the type of the limb, i.e. three-legged latticed specimens with a larger D_s/T_s are more vulnerable to damage due to the weaker confinement from the tube in the limb to its core concrete.

From the tests, it was observed that the failure process of single limb (C1) on one side of the centroid axis was different from that of the corresponding double limbs (C2 and C3) on the other side of the centroid axis due to the different capacity of CFST limbs under tension and compression.

For CFST latticed specimens the tensile fracture and/or compressive buckling of single limb were formed obviously earlier than those of the corresponding double limbs; however, for steel latticed specimens the tensile fracture and/or compressive buckling of single limb were slightly earlier than those of the corresponding double limbs. This can be explained by that the difference in tensile and compressive performance of CFST limbs is obviously larger than that of steel tube limbs.

Fig. 8 shows the failure pattern of CFST and steel latticed specimens after the completion of tests. It can be seen that, in general, the fracture or/and buckling of the limbs in the specimens are observed at the location close to the bottom stiffeners; however, weld cracking appears at the top surface of baseplate of specimens Cb-0.05 and Cb-0.26, which has a certain effect on the performance while loaded in push loading direction due to the change of load-transfer mechanism. The damage of CFST latticed specimens with a larger n becomes more serious due to a greater second-order effect of axial compressive force. Under the same n value the damage of limbs in the CFST latticed specimens is severer than that in the steel counterparts based on the comparison of the fractures and buckles recorded in the tests. For specimens with D_s/T_s of 51.5, length and width of fracture in single limb of steel specimen are 2.5-3.0 times of those of CFST specimen, and length of buckles and buckling range in double limbs of steel specimen are 1.5-2.0 times of those of CFST specimen. For specimens with D_s/T_s of 24.9, length and width of fracture in single limb of steel specimen are $0.75 D_s$ and 5.38 mm respectively; however, there is no fracture in single limb of CFST specimen. Moreover, height of buckles and buckling range of double limbs in the steel specimen are 1.2-1.5 times of those in the CFST specimen. This means that the capacity of steel tube in the CFST limbs can be fully utilized owing to the existence of the filled concrete. Generally, only a few oblique lacings of four CFST latticed specimens and one steel latticed specimen possess overall out-of-plane deflection, i.e. one oblique lacing within the first internode of specimens Ca-0.26, Ca-0.52 and Sb-0.26, and five oblique lacings within the first two and the fourth internodes of specimens Cb-0.26 and Cb-0.52. This indicates that the lacings have larger influence on specimens with a smaller D_s/T_s and a larger n. Moreover, for CFST latticed specimens with D_s/T_s of

51.5, cracking in weld heat-affected zone near the bottom stiffeners causes the partial failure of connection between limb and lacings; however, there is no obvious damage to the connections of CFST latticed specimens with D_s / T_s of 24.9. This may be due to the fact that cracking of weld between single limb and bottom endplate with n of 0.05 and 0.26 and overall out-of-plane deflection of more oblique lacings of specimen with n of 0.52 reduce the connection stresses. Steel latticed specimens have no obvious connection damage owing to their more obvious fracture of single limb than the corresponding CFST latticed specimens, which can also play a role in reducing the connection stresses.

3.2. Load versus deformation curves

The lateral load (P) versus lateral displacement at the top of specimen over the height (Δ_{top} / H) hysteretic curve of all specimens is plotted in Fig. 9 by the solid line, where '○' denotes the starting of the tube fracture of the limb or the weld cracking (see Fig. 8). It can be seen that, the bearing capacity of the specimens decreases quickly below 80% of the maximum bearing capacity once fracture of the limb or weld cracking happens, and thus the fracture of the limb or weld cracking is considered to be a failure ultimate for the specimens. Irrespective of D_s / T_s and n values, $P - \Delta_{top} / H$ hysteretic curve of CFST latticed specimens exhibits obvious asymmetric characteristics, and plumper hysteretic loops of a specimen are achieved while under pull loadings than under push loadings. The limb fracture of a CFST latticed specimen occurs in single limb (C1) when subjected to push loadings. These are obviously different from the observations of two-legged and four-legged CFST latticed specimens subjected to cyclic loadings (Kawano et al. 1996; Deng 2012; Luo 2013; Chen et al. 2014; Huang 2015; Yuan et al. 2016)[4-9]. This indicates that, for three-legged CFST specimens, single limb on one side of the centroid axis should have the similar compressive and tensile response as double limbs on the other side of the centroid axis. However, for steel latticed specimens, the difference in $P - \Delta_{top} / H$ hysteretic curve under push and pull loadings is smaller than that exhibited in the CFST latticed specimens. The difference in the

hysteretic curves between CFST and the corresponding steel latticed specimens is caused by the fact that, under the same dimensions and material properties, the different property in tension and compression of CFST members is much greater than that of steel members, which produces the different distance between centroid of limbs and the centroid axis of overall section in two loading directions. The lateral bearing capacities (P_{ue+} and P_{ue-}) defined as the peak load recorded in the tests are listed in Table 2.

Fig. 10 plots the $P - \Delta_{top} / H$ backbone curve of the tested specimens. It can be seen that, for CFST latticed specimens, the axial compression ratio (n) not only affects the bearing capacities but also determines the initial slope and ductility. Furthermore, under the same n value, CFST latticed specimen has obviously larger bearing capacity, initial slope and ductility compared with the corresponding steel latticed specimen owing to the existence of the filled concrete in the limbs, which has good interaction with its outer steel tube (Han et al. 2014)[1]. It can also be seen from Figs. 9 and 10 that, most of the hysteretic curves have a descending stage followed by a re-ascending stage in push loading direction; however, this phenomenon does not appear in pull loading direction. This may be due to the fact that, in push loading direction all lacings gradually participate in carrying the tensile forces after tube fracture of single limb (C1); however, in pull loading direction the stress of double limbs (C2 and C3) fails to reach hardening stage, which is partially demonstrated in Fig. 11, i.e. the strain of double limbs (C2 and C3) can steadily grow to about twice the strain corresponding to the tube fracture of single limb (C1).

The comparison of lateral load (P) versus strain (ε) hysteretic curves at the predetermined three points (see Fig. 3) between CFST and the corresponding steel latticed specimens is illustrated in Fig. 11, where ε_y is the yield strain of steel, and the capital letters 'L' and 'T' denote the longitudinal and transverse strains, respectively. It can be seen that, the $P - \varepsilon$ hysteretic curves of three positions are generally stable, and no abrupt changes occur. Both longitudinal and transvers strain developments at positions A and B exhibit the characteristics subjected to compression and bending, i.e. the hysteretic loops bias towards tension or compression side, and the maximum strain is larger

than ε_y except for the transverse strain of specimen Sa-0.26. At position E, the longitudinal strain development of steel latticed specimen is nearly symmetrical whilst CFST latticed specimen has an evident asymmetric longitudinal strain development, which is similar to the change in $P - \Delta_{top} / H$ hysteretic curves. The maximum strain at position E is smaller or slightly larger than ε_y. Under the same n value, specimens with a smaller D_s / T_s possess a more sufficient strain development regardless of the type of the limb and the CFST latticed specimens lead to a relatively fully developed strain value compared with the steel latticed specimens because the steel tube of CFST limbs could be made full use of owing to its interaction with the filled concrete.

The effect of parameters considered in the tests on lateral load ratio (p) versus longitudinal strain (ε) backbone curves at the predetermined three points is plotted in Fig. 12, where the red and blue lines represent the results under push and pull loadings, respectively. It can be seen that, for CFST latticed specimens, the effect of n and D_s / T_s on the changing rules of $p - \varepsilon$ curves of the limbs is different in two loading directions, and generally specimens with a larger n value have a larger compressive strain in pull loading direction and a smaller tensile strain in push loading direction under the same lateral load ratio (p) due to the response difference in two loading directions. Steel latticed specimens possess similar trend of $p - \varepsilon$ curves of the limbs as CFST latticed specimens; however, under the same p value compressive strain in pull loading direction and tensile strain in push loading direction of CFST latticed specimens are larger than those of the steel counterparts as a larger initial compressive strain is produced in the CFST limbs. Furthermore, for $p - \varepsilon$ curves at position E, the discrepancy is mainly from the difference in the initial compressive strain due to axial compressive force and there is no obvious difference in the curve trends except for the results of specimen Ca-0.52, which results in an evident increasing in the compressive strain in both loading directions due to the extremely serious deterioration of the limbs near the bottom stiffeners, as shown in Fig. 8(a4).

3.3. Bearing capacity

Fig. 13 shows the effect of parameters on lateral bearing capacities. It can be seen that, under the same n value, specimens with a lower D_s/T_s exhibit a larger bearing capacity in both loading directions irrespective of the type of the limb due to the increase of steel area and confinement of steel tube to its core concrete, and the bearing capacities of CFST latticed columns are obviously higher than those of the steel counterparts owing to the composite action between steel tube in the limbs and its core concrete. P_{ue+} (P_{ue-}) of CFST latticed specimens with D_s/T_s of 51.5 and 24.9 is 85.9% (248.0%) and 18.7 (37.1%) higher than those of the steel counterparts, respectively. For CFST latticed specimens, P_{ue-} shows increasing and decreasing trends before and after n =0.26, respectively; however, P_{ue+} increases with increasing n. The increased bearing capacities of CFST latticed specimens are due to the fact that, when n is relatively small (about 0.26 in the current tests), the constraint of axial compression to the tensile stress in the limbs caused by the lateral cyclic loadings increase with increase of n. Compared with the corresponding CFST latticed specimens with n of 0.26, the decreased P_{ue-} of CFST latticed specimens with n of 0.52 in pull loading direction is caused by the increased second-order effect under axial compression, and the increased P_{ue+} of CFST latticed specimens with n of 0.52 in push loading direction may be induced by the increased constraint of axial compression to the premature tensile fracture of the single limb (C1).

3.4. Initial stiffness

The average initial stiffness (S_i) of the tested specimens in two loading directions is given in Table 2. The variation of S_i is demonstrated in Fig. 14. It can be seen from Table 2 and Fig. 14 that, S_i increases with decrease of D_s/T_s regardless of the type of the limb because of the increased moment of inertia of steel section, and CFST specimens have a larger S_i value compared to the steel counterparts due to the existence of the concrete core in the limbs. S_i of CFST latticed specimens with D_s/T_s of 51.5 and 24.9 is 88.2% and 37.7% higher than that of the steel

counterparts, respectively. Moreover, owing to the increased inhibiting effect of axial compressive force on the tensile stresses in the limbs caused by the lateral cyclic loadings, S_i of CFST latticed specimens increases with increasing n.

3.5. Accumulated energy dissipation

The area surrounded by the complete hysteretic loops of $P - \Delta_\mathrm{top}$ curve during each step is used to assess the accumulated energy dissipation capacity of the specimens (ATC 24 1992)[12]. Fig. 15 shows the comparison of the accumulated energy dissipation (E) of CFST and steel latticed specimens with increasing Δ_top / H, and the specimen is considered to have lost its energy dissipation ability while the fracture of the limb or weld cracking appeared. It can be seen that, generally, specimens with a smaller $D_\mathrm{s} / T_\mathrm{s}$ have a larger E regardless of the type of the limb and CFST latticed specimens have a larger E compared to the steel counterparts. This is due to the increase of both bearing capacity and initial stiffness with decrease of $D_\mathrm{s} / T_\mathrm{s}$ and the existence of the filled concrete in the limbs, which generates plumper hysteretic loops in both loading directions. Moreover, under the same Δ_top / H value E of CFST latticed specimens decrease with increase of n due to the increased second-order effect of axial compression.

4. Finite element analysis (FEA) modelling

4.1. General description of FEA model

As mentioned earlier, numerical study on the seismic behaviour of four-legged CFST latticed members has been performed (Deng 2012; Luo 2013; Huang 2015; Yuan et al. 2016) [4,6,7,9], and there is little numerical work reported for three-legged CFST latticed members subjected to cyclic loadings. In this study, a nonlinear finite element analysis (FEA) model was constructed by ABAQUS/Standard solver [15] to simulate the responses of three-legged CFST latticed columns subjected to constant axial compressive force and lateral cyclic loadings.

4.2. Details of FEA model

It is shown that stress versus strain backbone curve of structural steel under cyclic loading is

remarkably different from that subjected to monotonic loading mainly due to the improved strain hardening effect and decreased ductility (Shi et al. 2011; 2012)[16,17]. Thus, the accuracy of the simulation on stress versus strain backbone curve of structural steel under cyclic loading directly determine the preciseness of the FEA modelling results. In this study, the metal plasticity model in ABAQUS [15] using the Mises yield surfaces with the associated plastic flow was chosen to replicate the mechanical behaviour of steel tube in the limbs and tube lacings, and the mixed hardening model incorporating both isotropic hardening and nonlinear kinematic hardening provided in ABAQUS [15] was also adopted.

For the isotropic hardening model of steel, the development of the yield surface size (σ^0) is defined as a function of the equivalent plastic strain ($\overline{\varepsilon}^{pl}$):

$$\sigma^0 = \sigma\big|_0 + Q_\infty \cdot (1 - e^{-b \cdot \overline{\varepsilon}^{pl}}) \tag{5}$$

where, $\sigma\big|_0$ is the yield stress corresponding to zero plastic strain, Q_∞ is the maximum variation of the dimension of the yield surface and b represents the rate at which the dimension of the yield surface varies as plastic straining develops.

For the nonlinear kinematic hardening model of steel, the back stress vector (α_k) describing the transition of the yield surface in stress space is defined as a function of the plastic strain (ε^{pl}):

$$\alpha_k = \frac{C_k}{\gamma_k} \cdot (1 - e^{-\gamma_k \cdot \varepsilon^{pl}}) + \alpha_{k,1} \cdot e^{-\gamma_k \cdot \varepsilon^{pl}} \tag{6}$$

where, C_k is the initial kinematic hardening modulus, γ_k determine the rate at which the kinematic hardening modulus decreases with increasing plastic deformation, and $\alpha_{k,1}$ denotes the kth back stress vector at the first data point (initial value of the kth back stress).

Shi et al. (2012)[17] investigated the performance of structural steel under cyclic loading through tests, and further derived the mixed hardening parameters from the measured and calculated data. In this study, the cyclic hardening parameters of steel tube in the limbs and tube lacings were obtained by the linear interpolation of the results suggested by Shi et al. (2012)[17] according to the yield

stress corresponding to zero plastic strain ($\sigma|_0$) and calibrated by the measured results of three-legged CFST latticed specimens, as presented in Table 5, where four back stresses are considered for the nonlinear kinematic hardening model.

To accurately simulate the fracture failure of limbs during the tests, the ductile damage (fracture) of steel was considered in the FEA model. While defining the ductile damage of steel, the relationship between the fracture initiation strain and the stress triaxiality suggested in Yu and Jeong (2010)[18] was adopted as the damage initiation criterion, and the function between the damage variable (d_s) and the plastic displacement ratio ($\overline{u}^{pl}/\overline{u}_f$) presented in Zhou et al. (2014)[19] was adopted as the damage evolution criterion, as given in the following equation:

$$d_s = 1.3(\overline{u}^{pl}/\overline{u}_f)^{7.6} \tag{7}$$

where, $\overline{u}^{pl}$ is the plastic displacement, and $\overline{u}_f$ is the ultimate displacement at failure.

The cyclic stress (σ_s) versus strain (ε_s) relationship for structural steel with progressive damage degradation is schematically demonstrated in Fig. 16, where E_s is the elastic modulus of steel, σ_{sd} and $\overline{\varepsilon}_{s0}^{pl}$ are the stress and equivalent plastic strain at the onset of damage, and $\overline{\varepsilon}_{sf}^{pl}$ is the equivalent plastic strain at failure.

In the modelling, the steel tubes of the specimens had an elastic modulus of 2.06×10^5 N/mm^2 and a Poisson's ratio of 0.3. Both endplates, stiffeners, loading plate, rollers and connector were set to be elastic material with elastic modulus of 1.0×10^{12} N/mm^2 and Poisson's ratio of 0.001.

The concrete damaged plasticity model in ABAQUS [15] was adopted to simulate the nonlinear behaviour of core concrete under cyclic loading, which can describe the stress versus strain backbone curve, the degradation of the elastic stiffness due to the damage accumulation, the stiffness recovery when the load changes from tension to compression and vice versa and the plasticity parameters.

For concrete subjected to compression, the nonlinear stress versus non-elastic strain relationship needs to be defined, which can be derived from the relationship of engineering stress versus

engineering strain of core concrete in CFST presented in Han et al. (2007)[20] with the confinement effect of steel tube considered. The compressive engineering stress (σ_c) versus engineering strain (ε_c) relationship of concrete is as follows:

$$\frac{\sigma_c}{f_c'} = \begin{cases} 2(\varepsilon_c / \varepsilon_0) - (\varepsilon_c / \varepsilon_0)^2 & (\varepsilon_c \leq \varepsilon_0) \\ \dfrac{\varepsilon_c / \varepsilon_0}{\beta \cdot (\varepsilon_c / \varepsilon_0 - 1)^2 + \varepsilon_c / \varepsilon_0} & (\varepsilon_c > \varepsilon_0) \end{cases} \tag{8}$$

where, $\varepsilon_0 = (1300 + 12.5 f_c' + 800 \xi^{0.2}) \cdot 10^{-6}$, $\beta = (2.36 \times 10^{-5})^{[0.25 + (\xi - 0.5)^7]} \cdot (f_c')^{0.5} / 2 \geq 0.12$, f_c' is the cylinder compressive strength of concrete from f_{cu} of SCC when tests conducted according to the suggested relationship between them in EN1992-1-1 (2005)[21] and ξ is the confinement factor (Han et al. 2007)[20].

For concrete under tension, the stress versus cracking displacement model suggested by Goto et al. (2010)[22] was incorporated into ABAQUS to simulate the tension stiffening effect. The tensile strength of the concrete (σ_{t0}) equals to 10% of the peak compressive stress in this study.

The concrete damaged plasticity model assumes that the degradation of elastic stiffness induced by plastic straining both in tension and compression is characterized in terms of two damage variables (i.e. compression damage factor d_c and tension damage factor d_t), which are the function of the stress state and the uniaxial damage variables. Based on the iterative calculation, it was found that the calculation convergence could be well achieved by the equation of compression damage factor d_c suggested by Birtel and Mark (2006)[23]:

$$d_c = 1 - \frac{\sigma_c \cdot E_c^{-1}}{\varepsilon_c^{pl} \cdot (1 / b_c - 1) + \sigma_c \cdot E_c^{-1}} \tag{9}$$

where, σ_c is the compressive stress, E_c is the elastic modulus, and b_c is the ratio of plastic strain over non-elastic strain and equals to 0.7 in this study.

To ensure the convergence and precision of the FEA modelling, the tension damage factor d_t was calculated using the equation suggested by Goto et al. (2010)[22]:

$$d_t = \frac{1.24k_t}{\sigma_{t0}} \cdot u_t^{ck} \le 0.99 \qquad (10)$$

where, σ_{t0} is the tensile strength, u_t^{ck} is the cracking displacement, and k_t is the slope of the stress versus cracking displacement curve.

The recovery of the tensile and compressive stiffness subjected to load reversal was adopted to consider the opening and closure of microcracks within core concrete in the limbs. The compression stiffness recovery factor (w_c) and the tension stiffness recovery factor (w_t) were set to be 0.2 and 0.0 respectively, which had been successfully adopted in the simulation of cyclic behavior of recycled aggregate concrete filled steel tube beam-columns (Yang 2015)[24]. Therefore, the compressive stiffness of the concrete core in the limbs partially recovered (which in this case was 20% of the initial undamaged stiffness) and no tensile stiffness recovery was considered.

In the FEA simulation, the Poisson's ratio of concrete was set to be 0.2 (Goto et al. 2010; Yang 2015; Ma et al. 2018)[22, 24, 25] and the elastic modulus of concrete (E_c) was determined by the formula in ACI 318-11 (2011)[26]:

$$E_c = 4730\sqrt{f_c'} \qquad (N/mm^2) \qquad (11)$$

Furthermore, the plasticity parameters of concrete used in the FEA model were based on the results by Goto et al. (2010)[22] and individually calibrated according to the current experimental results, as given in Table 6, where θ is the dilation angle, e is the eccentricity of flow potential, f_{b0}/f_{c0} is the ratio of initial equibiaxial compressive yield stress to initial uniaxial compressive yield stress, K_c is the ratio of the second stress invariant on the tensile meridian to that on the compressive meridian, and μ is the viscosity parameter. The cyclic stress (σ_c) versus strain (ε_c) relationship of core concrete in the limbs is schematically demonstrated in Fig. 17.

In the model, three-dimensional shell elements with 4-node reduced-integration (S4R) were selected to model the steel tube in the limbs and tube lacings. The Simpson integration with 9 integration points was adopted along the thickness of the shell elements. Core concrete in the limbs,

two endplates, stiffeners, loading plate, rollers and connector were simulated using three-dimensional brick elements with 8-node reduced-integration (C3D8R). Due to irregularity of the oblique lacings, the mesh density has a great impact on the convergence of the calculation using FEA model. The structured meshing technology was adopted, and gradually refined meshing was performed to inspect the mesh convergence, until the discrepancy of FEA modelling between two adjacent mesh densities was less than 5%. Moreover, local encryption within the lower 150 mm of the limbs was adopted to accurately capture the fracture process of steel tube. Mesh density applied to the specimens is listed in Table. 7. After the completion of mesh convergence study, the eventual meshing of three-legged CFST latticed columns with the calculation accuracy and efficiency satisfied was accomplished, as shown in Fig. 18.

The surface to surface contact with finite sliding available in ABAQUS [15] was chosen to model the contact between steel tube in the limbs and its core concrete, and the inner wall of steel tube in the limbs and surface of core concrete were defined as master and slave surface, respectively. The surface to surface contact was achieved by ensuring the coincidence of nodes of steel tube and its core concrete at the same position (i.e. having the same normal and tangential directions) and building the contact algorithm based on the 'finite slippage' to strengthen the constraints in the normal and tangential directions. The contact properties along normal and tangential directions of interface between steel tube in the limbs and its core concrete were set to be the 'hard contact' and 'Coulomb friction' with friction coefficient of 0.6 (Ma et al. 2018)[25], respectively. In ABAQUS, the recommended value for the friction coefficient between two surfaces is 0-0.6, and three values were adopted in the FEA modelling, i.e. 0.2, 0.4 and 0.6. It was found that the simulated hysteretic behaviour of three-legged CFST latticed columns with friction coefficient of 0.6 was closer to the experimental results than that with other two friction coefficients. The node to surface contact with small sliding in ABAQUS [15] was adopted to simulate the contact between the rollers and connector (loading plate), and there was only 'hard contact' between them. The 'Tie' constraint in ABAQUS [15] was used to simulate the welds between steel tube in the limbs and tube lacings, the

contact between CFST limbs and both endplates and the contact between stiffeners and steel tube in the limbs (bottom endplate). Moreover, the rollers and the loading plate were connected as a whole by the 'Tie' constraint to improve the calculation convergence, although the limited free rolling happened to the rollers in the tests.

All degrees of freedom (DOFs) of bottom endplate were restrained to replicate the fixed boundary conditions in the tests. The translational displacements at X and Y direction and rotations at X and Z direction of barycenter line on the loading plate were restricted except for the translational displacements at Z direction and rotations at Y direction. Two reference points, including one located above the barycenter of specimen cross-section coincided with the loading plate and another located on the side of the centroid of the vertical plate of connector coupled with the vertical plate of connector, were set. The constant axial compressive force was first applied on the reference point coincided with the loading plate, and then the cyclic horizontal displacements (Δ_{top}) were acted on the reference point coupled with the vertical plate of the connector. The adopted boundary conditions for a typical three-legged CFST latticed column under lateral cyclic loadings are shown in Fig. 18. The responses of the model were obtained by the Newton-Simpson's method.

4.3. Comparison between the simulated and measured results

Fig. 19 demonstrates the predicted failure pattern of three-legged CFST and steel latticed specimens under lateral cyclic loadings, where only specimen Cb-0.52 has no tube fracture. It can be seen from the comparison between Fig. 19 and Fig. 8 that, in general, the predicted failure range, fracture and deformation pattern of the limbs and out-of-plane deformation of the tube lacings of the specimens with a larger n are in good agreement with the experimental results. The comparison between the predicted and measured $P - \Delta_{\text{top}} / H$ and $P - \varepsilon$ hysteretic curves is shown in Fig. 9 and Fig. 20, respectively, where 'Δ' stands for the predicted starting of the tube fracture of the limb in Fig. 9. It can be observed that a reasonably good agreement is obtained between both results. However, there are actually certain differences between the numerical and experimental hysteretic curves. This can

be explained by the following reasons: 1) initial imperfection and performance variability of materials always exists in the tested specimens; 2) constant axial compression applied to the top endplate of the specimens is hard to be realized through the loading process due to the deviation of axial compressive forces (see Fig. 4); 3) load eccentricity may be introduced to the specimens due to manufacturing deviation; and 4) there are weld residual stress and heat affected zone in the joints between limb and lacings. These factors cannot be completely taken into account in the FEA model. The comparison between the numerical and experimental bearing capacities is indicated in Fig. 21 and Table 2. It can be found that a good agreement between P_{uc} and P_{ue} is attained as the mean value and standard deviation of P_{uc} / P_{ue} are 1.012 and 0.105, respectively.

4.4. Effect of typical parameters on $P - \Delta_{top}$ hysteretic curves

To confirm the universality of the FEA model and analyze the influencing law of parameters which are not considered in the tests, the verified FEA model was further adopted to investigate the effect of typical parameters on $P - \Delta_{top}$ hysteretic curves of three-legged CFST latticed columns with one end fixed and another end free, and the modelling results are plotted in Fig. 22. It should be noted that, the effect of ductile damage (fracture) of steel is not included in the parametric analysis because the parameters for the ductile damage (fracture) of steel need to be determined by the tests of material property. The basic computing conditions were: D_s=100 mm, D_s / T_s=41.7, D_w=34 mm, D_w / T_w=15, H=4500 mm, $f_{ys} = f_{yw}$=345 MPa, f_{cu}=60 MPa, H / l_w=10, l_w / h_0=1.09, and n=0.4. The calculated bearing capacities (P_{ue+} and P_{ue-}), initial stiffness (K_i) and accumulated energy dissipation while Δ_{top} equal to 100 mm (E_t) under different parameters are presented in Table 8. It can be seen from Fig. 22 and Table 8 that, similar to the measured results in this study, the simulated $P - \Delta_{top}$ hysteretic curves possess different backbone curve in two loading directions. Generally, D_s / T_s, f_{ys}, H / l_w, l_w / h_0 and n have remarkable impact on the $P - \Delta_{top}$ hysteretic curves and mechanical index of three-legged CFST latticed columns subjected

to lateral cyclic loading, and the P_{ue+} (P_{ue-}), K_i and E_t increase with decrease of D_s / T_s, H / l_w and l_w / h_0 and increase of f_{ys} and n. The effect of key parameters on cyclic performance of three-legged CFST latticed columns can provide a reference for the follow-up experimental and theoretical research.

5. Conclusions

Experimental and numerical investigation on the performance of three-legged CFST and steel columns subjected to constant axial compressive force and lateral cyclic loadings is presented in this study. Based on the tests and the analytical results, the following conclusions can be obtained:

(1) CFST latticed specimens have better hysteretic performance than the steel counterparts; however, three-legged CFST latticed specimens generally demonstrate different behaviour in two loading directions owing to the different property of the CFST members under tension and compression.

(2) Failure pattern of all specimens is either fracture or buckling of limbs or both at the section close to the bottom stiffeners and failure of oblique lacings, and CFST latticed specimens have severer limb damage and more oblique lacings failure than the steel counterparts. The damage becomes more serious for CFST latticed specimens with a larger n. Failure of connection between limb and lacings happens to CFST latticed specimens with D_s / T_s of 51.5, and steel latticed specimens have no obvious connection damage.

(3) For CFST latticed specimens, $P - \Delta_{top} / H$ hysteretic curve is asymmetric in two loading directions and the hysteretic loops in pull loading direction are plumper than those in push loading direction. However, steel latticed specimens have almost symmetric $P - \Delta_{top} / H$ hysteretic curve in both loading directions. Moreover, the obtained $P - \varepsilon$ hysteretic curves of all specimens are generally stable and no sudden changes occur.

(4) P_{ue}, S_i and E of the specimens increase with decreasing D_s / T_s irrespective of the type of the limb. CFST latticed specimens have a larger P_{ue}, S_i and E than the steel counterparts due

22

to the composite action between steel tube in the limbs and its core concrete. CFST latticed specimens with a larger n have a larger P_{ue+} and S_i and a lower E. Moreover, P_{ue-} of CFST latticed columns shows increasing and decreasing trends before and after $n=0.26$, respectively.

(5) The modelling results of three-legged CFST and steel latticed columns subjected to cyclic loadings by the FEA model constructed in this study achieved good agreement with the experimental observations, and the effect of typical parameters on $P-\Delta_{top}$ hysteretic curve of three-legged CFST latticed columns under lateral cyclic loadings is further investigated.

It is clear that, for three-legged CFST latticed columns under lateral cyclic loadings, the tensile fracture of single limb is formed earlier than that of the corresponding double limbs when all limbs have the same dimensions and material properties. It is necessary to reasonably match geometric and physical parameters of steel tube and its core concrete in the limbs of three-legged CFST latticed columns to achieve equal or similar tensile and compressive property of single limb and the corresponding double limbs, and accordingly stable and almost symmetric hysteretic performance in both loading directions can be obtained. In the future, experimental and numerical investigation on the cyclic responses of three-legged CFST latticed columns under different material and geometric property of limbs, H/l_w, l_w/h_0 and n needs to be further carried out. With the progress of experimental and theoretical research, the failure criterion of three-legged CFST latticed members subjected to lateral cyclic loadings and the restoring force model for the elastoplastic seismic response analysis and dynamic time history analysis of structures including three-legged CFST latticed members can be established, which will provide the basis for developing a reasonable seismic design method of such composite structures.

Acknowledgements

References

[1]   Han LH, Li W, Bjorhovde R. Developments and advanced applications of concrete-filled steel tubular (CFST) structures: members. Journal of Constructional Steel Research, 2014, 100: 211-228.

[2]   Kawano A, Sakino K. Seismic resistance of CFT trusses. Engineering Structures, 2003, 25(5): 607-619.

[3]   Ou Z, Chen B, Hsieh KH, Halling MW, Barr PJ. Experimental and analytical investigation of concrete filled steel tubular columns. Journal of Structural Engineering ASCE, 2011, 137(6): 635-645.

[4]   Huang Y. Seismic behavior of concrete filled steel tubular built-up columns. Trento: University of Trento, 2015.

[5]   Kawano A, Matsui C, Sakino Y. An experimental study on the elasto-plastic behavior and deformability of concrete-filled tubular truss beam-columns under cyclic loading. Journal of Structural and Construction Engineering, Architectural Institute of Japan (AIJ), 1996, No. 482: 141-150. (in Japanese)

[6]   Deng X. Study on the seismic performance of concrete filled steel tubular lattice column. Master Thesis of Central South University, 2012. (in Chinese)

[7]   Luo Y. Studies on the seismic performance of four-tube concrete filled steel tubular laced columns. Master thesis of Central South University, 2013. (in Chinese)

[8]   Chen B, Zou Y, Tang C, Yang X, He M. Contrast research on square and circular CFST laced columns pseudo-static test. China Civil Engineering Journal, 2014, 47(S2): 108-112. (in Chinese)

[9]   Yuan H, Wu Q, Chen B, Lyu Y. Aseismic performance test and FEM analysis of uniform sectional CFST lattice column with flat lacing tubes. Engineering Mechanics, 2016, 33(10): 226-235. (in Chinese)

[10] DBJ 13-51. Technical specification for concrete- filled steel tubular structures. Fujian: Department of Construction of Fujian Province, 2003. (in Chinese)

[11] GB 50017. Code for design of steel structures. Beijing: China Architecture & Building Press, 2003. (in Chinese)

[12] ATC-24. Guidelines for cyclic seismic testing of components of steel structures. Redwood City (CA): Applied Technology Council, 1992.

[13] Varma AH, Ricles JM, Sause R, Lu LW. Seismic behavior and design of high-strength square concrete-filled steel tube beam columns. Journal of Structural Engineering ASCE, 2004, 130(2): 169-179.

[14] Zhou F, Xu W. Cyclic loading tests on concrete-filled double-skin (SHS outer and CHS inner) stainless steel tubular beam-columns. Engineering Structures, 2016, 127: 304-318.

[15] ABAQUS. ABAQUS Standard User's Manual, Version 6.14. Dassault Systèmes Corp., Providence, RI, 2014.

[16] Shi Y, Wang M, Wang Y. Experimental and constitutive model study of structural steel under cyclic loading. Journal of Constructional Steel Research, 2011, 67: 1185-1197.

[17] Shi Y, Wang M, Wang Y. Experimental study of structural steel constitutive relationship under cyclic loading. Journal of Building Materials, 2012, 15(3): 293-300. (in Chinese)

[18] Yu HL, Jeong DY. Application of a stress triaxiality dependent fracture criterion in the finite element analysis of unnotched Charpy specimens. Theoretical and Applied Fracture Mechanics 2010, 54(1): 54-62.

[19] Zhou T, Li W, Guan Y, Bai L. Damage analysis of steel frames under cyclic load based on stress triaxiality. Engineering Mechanics, 2014, 31(7): 146-155. (in Chinese)

[20] Han LH, Yao GH, Tao Z. Performance of concrete-filled thin-walled steel tubes under pure torsion. Thin-Walled Structures, 2007, 45(1): 24-36.

[21] EN 1992-1-1. Eurocode 2: Design of concrete structures, Part 1-1: General rules and rules for buildings. Comité Européen de Normalisation (CEN), Brussels, Belgium, 2004.

[22] Goto Y, Kumar G P, Kawanishi N. Nonlinear finite-element analysis for hysteretic behavior of thin-walled circular steel columns with in-filled concret. Journal of Structural Engineering ASCE, 2010, 136(11): 1413-1422.

[23] Birtel V, Mark P. Parameterised finite element modelling of RC beam shear failure. Proceedings of the 19th Annual International ABAQUS Users' Conference, Boston, USA, 2006, pp: 95-108.

[24] Yang YF. Modelling of recycled aggregate concrete-filled steel tube (RACFST) beam-columns subjected to cyclic loading. Steel and Composite Structures, 2015, 18(1): 213-233.

[25] Ma DY, Han LH, Li W, Zhao XL. Seismic Performance of Concrete-Encased CFST Piers: Analysis. Journal of Bridge Engineering ASCE, 2018, 23(1): 04017119.

[26] ACI 318-11. Building code requirements for structural concrete and commentary. Farmington Hills (MI), American Concrete Institute, Detroit, USA, 2011.

Tables:

Table 1. Summary of studies on seismic behaviour of CFST latticed columns.

No.	Cross-section	H (mm)	Dimension of limbs (mm) $D_s \times T_s$	Dimension of lacings (mm) $d_w \times t_w$	f_{ys} (MPa)	f_{cu} (MPa)	f_{yw} (MPa)	λ^*	n	Number of specimens	Ref.
1	Two-legged	2474	C: 60.5×2.3	C: 34.0×2.0	378	30.0	389	36.9	0~0.2	8	[5][+]
2	Four-legged	1200	C: 87×1.5	C: 48×2.5	315	43.7~60.0	/	20.1	0.2~0.4	8	[6][&]
3	Four-legged	1200~3000	C: 86×1.5	C: 48×2.0~3.0	315	20.4	320	19.4~41.5	0.2~0.3	6	[7][&]
4	Four-legged	1700	C: 90×3.4 S: 80×3.0	C: 42×2.7	259	71.7	259	29.6, 28.6	/	3	[8][+]
5	Four-legged	2500	C: 110×2.0	C: 50×2.0	345	40.3~57.5	374	37.1	0.15	6	[4][&]
6	Four-legged	2500	C: 114×2.0	C: 48×2.0	345	43.6~66.5	374	23.1	0.15	7	[9][&]

Notes: 1) 'C' and 'S' represent circular and square cross-section, respectively; 2) '+' means that only tests were carried out; and 3) '&' means that both tests and numerical simulation were performed.

Table 2. Information of the tested specimens.

No.	Label	D_s (mm)	T_s (mm)	D_s/T_s	H (mm)	l_w (mm)	h_0 (mm)	f_{cu} (MPa)	λ^*	n	N_0 (kN)	P_{ue+} (kN)	P_{ue-} (kN)	P_{uc+} (kN)	P_{uc-} (kN)	$\dfrac{P_{uc+}}{P_{ue+}}$	$\dfrac{P_{uc-}}{P_{ue-}}$	S_i (kN/m)
1	Sa-0.26	100	1.94	51.5	1960	320	320	--	29.4	0.26	144.0	41.9	-39.4	46.9	-35.3	1.119	0.896	2851
2	Ca-0.05	100	1.94	51.5	1960	320	320	55.9	34.2	0.05	79.0	47.0	-113.1	55.1	-113.5	1.172	1.004	3737
3	Ca-0.26	100	1.94	51.5	1960	320	320	55.9	34.2	0.26	395.0	77.9	-137.1	82.7	-130.1	1.062	0.949	5366
4	Ca-0.52	100	1.94	51.5	1960	320	320	55.9	34.2	0.52	780.0	110.5	-116.0	103.1	-122.9	0.933	1.059	6220
5	Sb-0.26	100	4.01	24.9	1960	320	320	--	32.6	0.26	260.0	102.7	-126.3	121.4	-107.8	1.182	0.854	4142
6	Cb-0.05	100	4.01	24.9	1960	320	320	55.9	40.6	0.05	104.5	108.1	-161.5	107.3	-152.2	0.993	0.942	4360
7	Cb-0.26	100	4.01	24.9	1960	320	320	55.9	40.6	0.26	522.5	121.9	-173.2	139.6	-159.5	1.145	0.921	5702
8	Cb-0.52	100	4.01	24.9	1960	320	320	55.9	40.6	0.52	1045.0	159.0	-156.5	143.0	-167.2	0.899	1.068	6750

Table 3. Properties of steel.

External diameter (mm)	Thickness (mm)	Yield strength (MPa)	Tensile strength (MPa)	Elastic modulus (N/mm^2)	Poisson's ratio	Elongation after fracture (%)
$D_s=100$	$T_s=1.94$	325.2	413.2	1.80×10^5	0.289	19.9
$D_s=100$	$T_s=4.01$	303.4	426.2	1.96×10^5	0.274	20.1
$d_w=34$	$t_w=2.46$	332.4	452.3	2.0×10^5	0.300	--

Table 4. Mix proportions and properties of the SCC.

Mix proportion (kg/m³)						Properties	
Cement	Fly ash	Coarse aggregate	Sand	Water	Water reducing agent	Slump (mm)	Spreading (mm)
420	130	832	800	184	6.3	270	660

Table 5. Cyclic hardening parameters of steel.

Dimension (mm)	$\sigma\|_0$ (MPa)	Q_∞ MPa	b	C_1 (MPa)	γ_1	C_2 (MPa)	γ_2	C_3 (MPa)	γ_3	C_4 (MPa)	γ_4
○-100×1.94	325.2	21	1.2	7636.6	174.6	6458.2	116.7	2885.0	33.6	1367.2	30.1
○-100×4.01	303.4	21	1.2	7244.2	174.2	6111.6	117.5	2919.0	33.2	1276.0	31.3
○-34×2.46	332.4	21	1.2	7766.2	174.8	6572.7	116.5	2873.7	33.8	1397.3	29.7

Table 6. Plasticity parameters of concrete.

θ	e	f_{b0}/f_{c0}	K_c	μ
30°	0.1	1.16	2/3	0.0005

Note: θ and μ are calibrated according to the current experimental results.

Table 7. Mesh density applied to the specimens.

Label	Details	Item						
		Tube in the limb	Concrete in the limb	Oblique lacing	Horizontal lacing	Endplate	Stiffener	Total model
Sa-0.26	Number of nodes	1620	/	240	110	768	340	26194
	Number of elements	1600	/	230	100	450	204	20968
	Mesh size (mm)	29.5×15 (15.0×7.5)	/	13.9×11.1	22.8×9.0	34.7×34.7×10	6.9×6.9×1.5	/
Ca series	Number of nodes	1620	4455	240	110	768	340	39559
	Number of elements	1600	3520	230	110	450	204	31528
	Mesh size (mm)	29.5×15 (15.0×7.5)	29.5×12.8×12.8 (12.8×12.8×7.5)	13.9×11.1	22.8×9.0	34.7×34.7×10	6.9×6.9×1.5	/
Sb-0.26	Number of nodes	1296	/	250	192	1083	400	25932
	Number of elements	1280	/	240	180	648	240	20340
	Mesh size (mm)	29.5×17.9 (17.9×7.5)	/	13.5×11.1	15.5×7.5	28.9×28.9×10	6.4×6.4×1.5	/
Cb series	Number of nodes	1296	3321	250	192	1083	400	35895
	Number of elements	1280	2560	240	180	648	240	28020
	Mesh size (mm)	29.5×17.9 (17.9×7.5)	29.5×14.4×14.4 (14.4×14.4×7.5)	13.5×11.1	15.5×7.5	28.9×28.9×10	6.4×6.4×1.5	/

Note: For the mesh size detail, the values in the brackets represent the results in the local encryption area.

Table 8. Computed results of three-legged CFST columns under different parameters.

Parameters	D_s / T_s			d_w / t_w			f_{ys} (MPa)			f_{yw} (MPa)			f_{cu} (MPa)			H / l_w			l_w / h_0			n		
	29.4	41.7	83.3	10	15	20	235	345	420	235	345	420	40	60	80	8	10	12	1.0	1.09	1.19	0.2	0.4	0.6
P_{ue+} (kN)	45.6	35.1	21.9	35.5	35.1	34.8	27.5	35.1	39.8	35.1	35.1	35.1	34.6	35.1	35.3	47.5	35.1	26.5	39.7	35.1	30.8	33.8	35.1	36.7
P_{ue-} (kN)	-38.2	-33.2	-25.6	-33.3	-33.2	-33.2	-27.2	-33.2	-36.3	-33.2	-33.2	-33.2	-30.6	-33.2	-35.7	-41.7	-33.2	-26.8	-36.2	-33.2	-30.2	-41.5	-33.2	-24.7
S_i (kN/m)	774	687	553	719	687	658	706	687	679	687	687	687	625	687	678	1288	687	399	816	687	577	727	687	567
E_t (kN.m)	20.8	19.3	14.8	20.1	19.3	18.6	20.0	19.3	17.1	19.3	19.3	19.3	19.4	19.3	19.3	35.7	19.3	9.5	22.9	19.3	16.1	19.6	19.3	19.4

Figures:
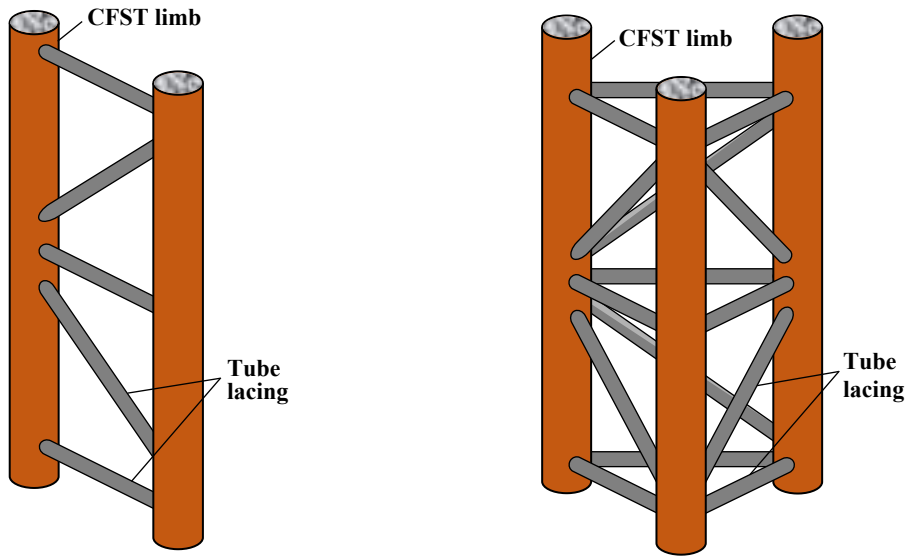
(a) Two-legged

(b) Three-legged
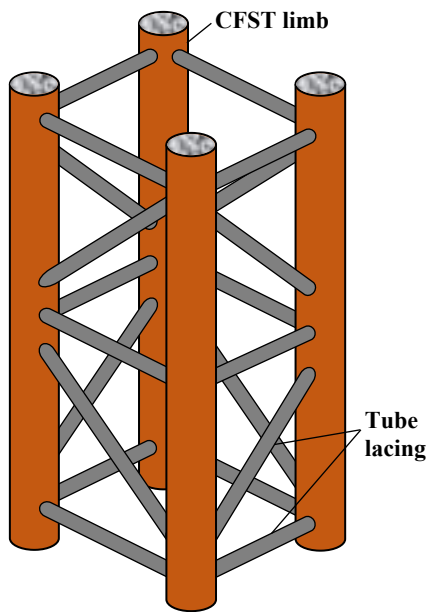
(c) Four-legged

Fig. 1. Typical CFST latticed members.
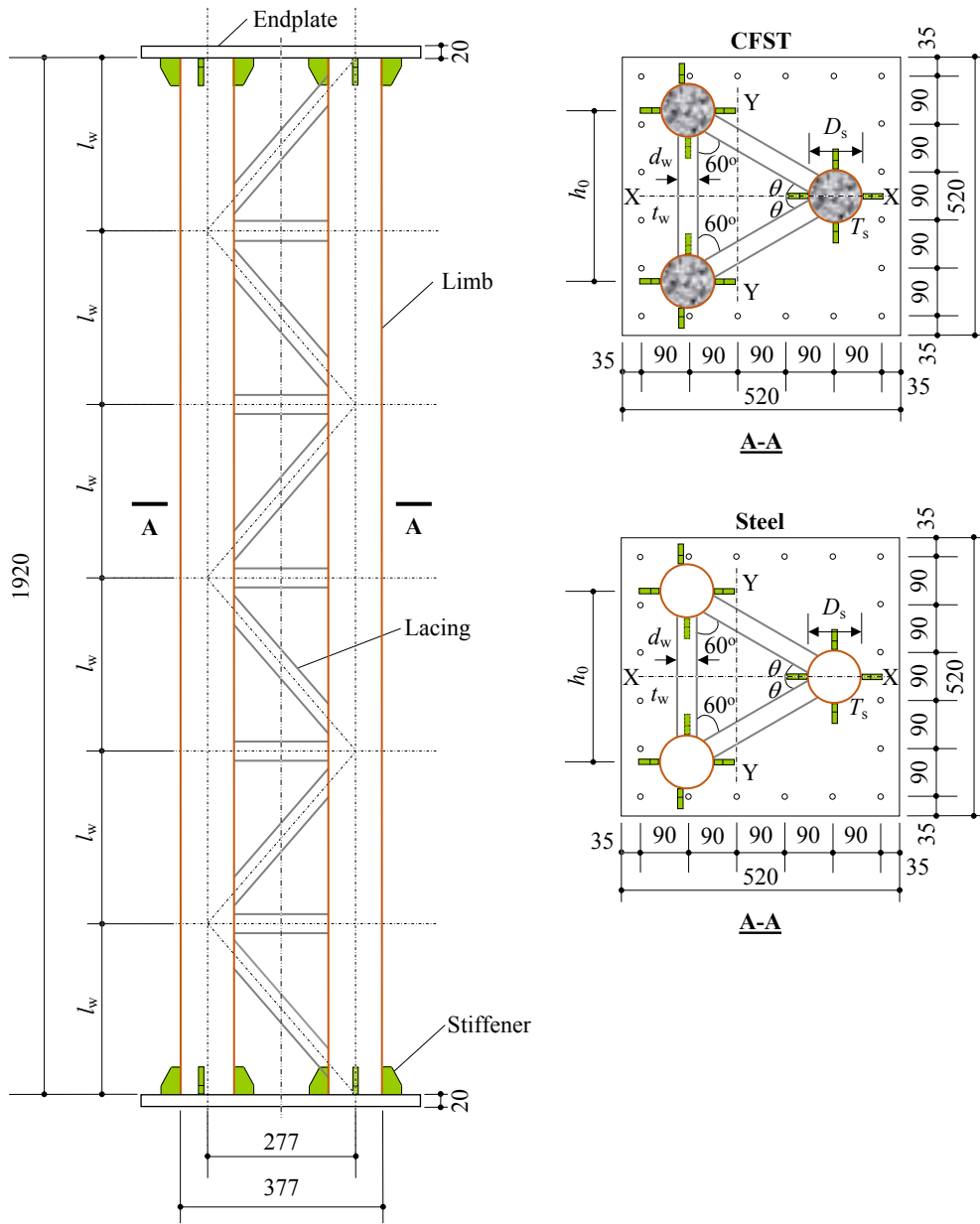
Fig. 2. Schematic diagram of the specimens. (unit: mm)

N_0

Actuator (2000 kN)

Restriction strip

Connector

Actuator (500 kN)

Roller

DT_0 (Δ_{top})

Push   Pull

C3   C1

Stiffener

340

1960

320

DT₂₅   DT₁₅

320

DT₂₄   DT₁₄

320

DT₂₃   DT₁₃

320

DT₂₂   DT₁₂

320

DT₂₁   DT₁₁

340

Reaction beam

E

B   A   80

Baseplate

Ground

Anchor rod

High-strength bolt

25 35 35

46   50 50 120 105

84 84 50

42

520   160

Roller system

C2

C1 A

DT₀

B   C3   E

DT_{t1}   DT_{t2}

Top view of specimens

Deformation transducer (DT)

Strain gauge

(a) Schematic view

33

(b) Real scenario

Fig. 3. Test set-up and instruments. (unit: mm)
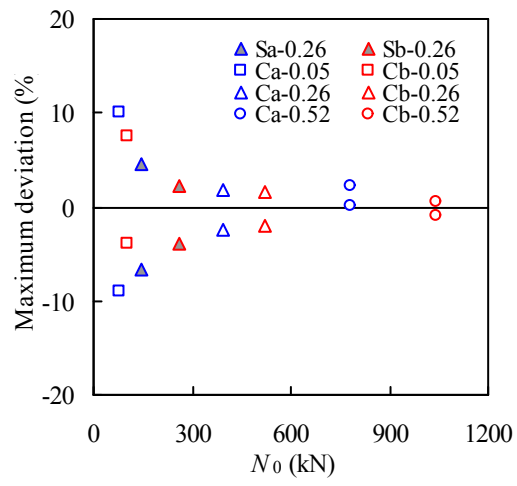
Fig. 4. Maximum deviation of axial compressive forces.
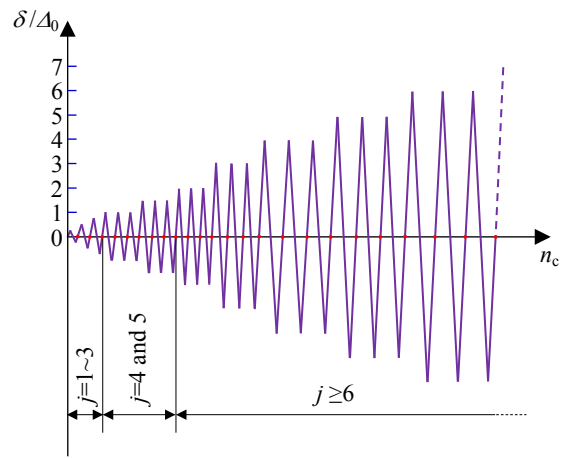
Fig. 5. Loading protocol.
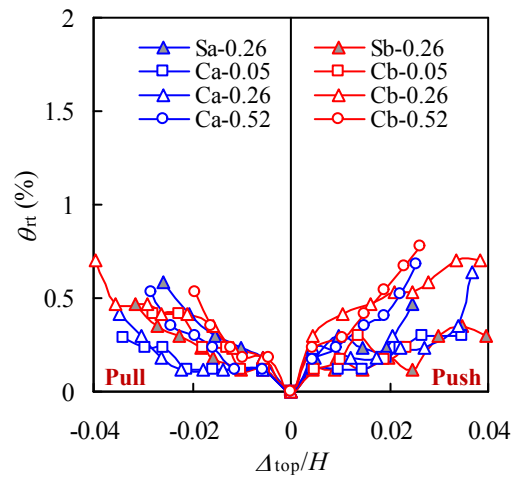
Fig. 6. Variation of relative torsion angle of the top endplate.
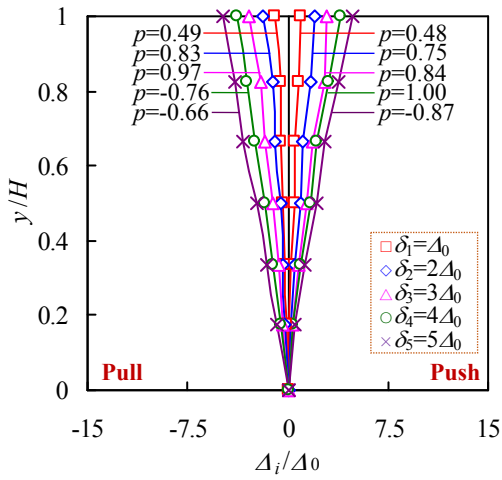
(1) Sa-0.26
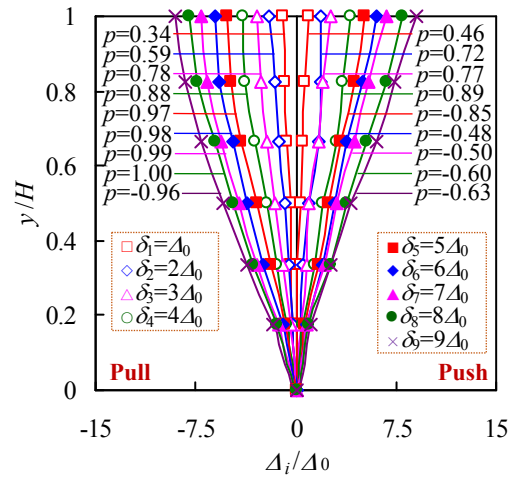
(2) Ca-0.26

(a) $D_s/T_s=51.5$
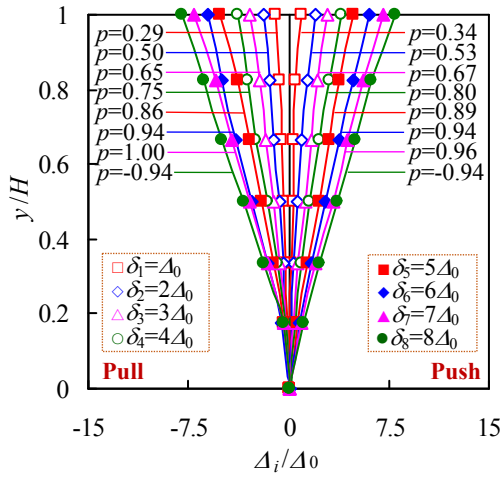
(1) Sb-0.26
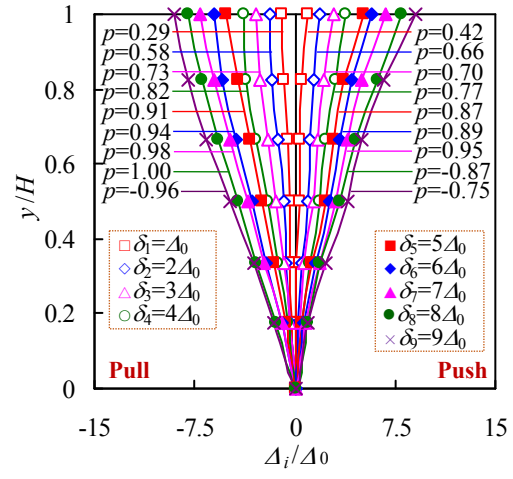
(2) Cb-0.26

(b) $D_s/T_s=24.9$

Fig. 7. Overall lateral displacements of the typical specimens.

(1) Sa-0.26

(2) Ca-0.05

(3) Ca-0.26

(4) Ca-0.52
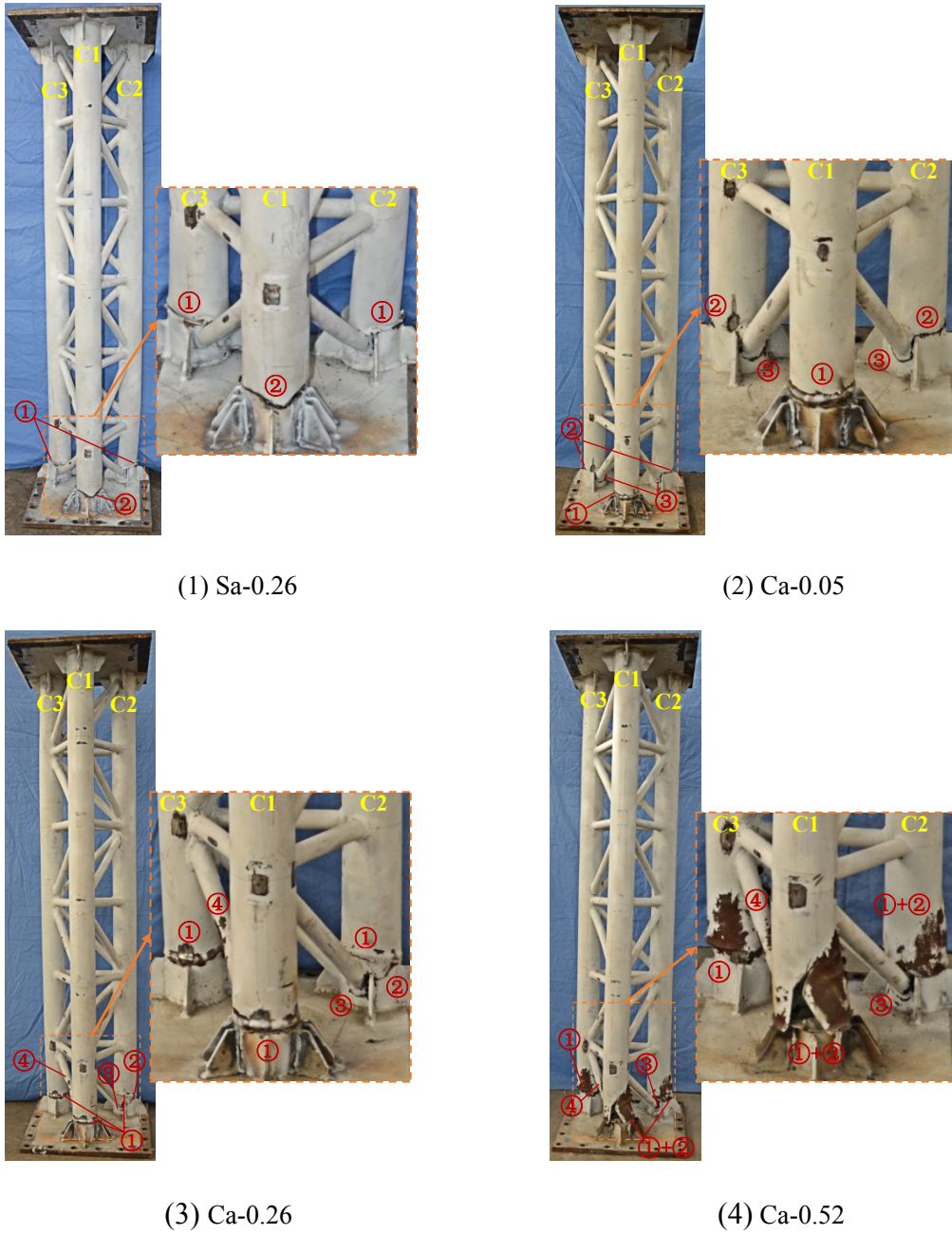
(a) D_s/T_s=51.5

Fig. 8. (Continued)

(①-Tube buckling of limb; ②-Tube fracture of limb; ③-Connection damage; ④-Overall out-of-plane deflection of lacing; ⑤-Weld cracking)
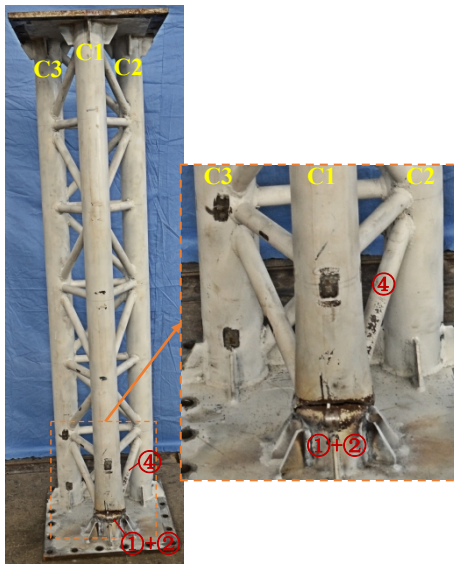
(1) Sb-0.26   (2) Cb-0.05
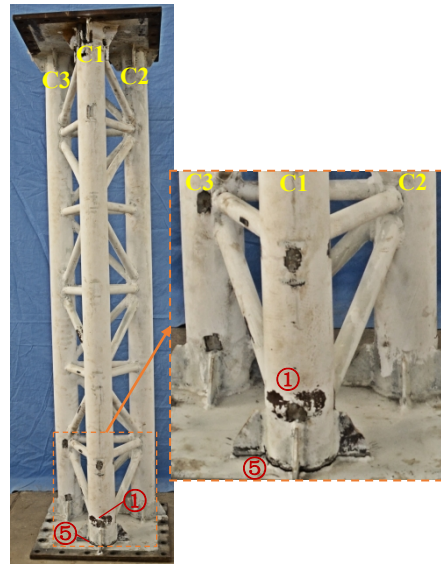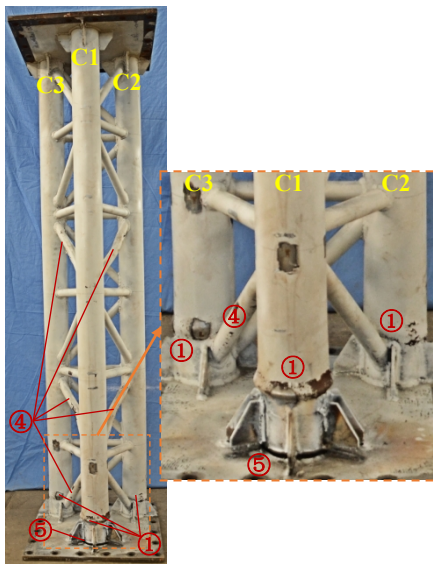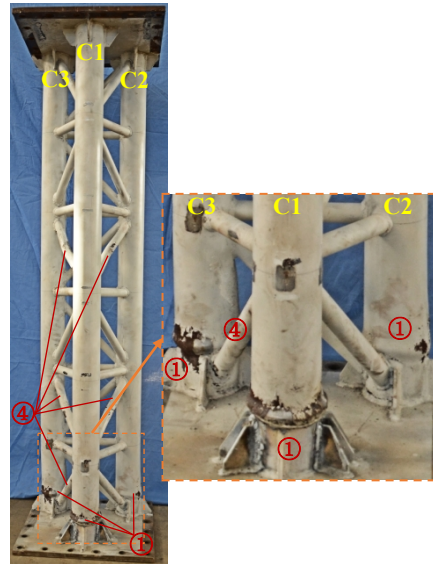
(3) Cb-0.26   (4) Cb-0.52

(b) D_s/T_s=24.9

Fig. 8. Failure pattern of the tested specimens.

(①-Tube buckling of limb; ②-Tube fracture of limb; ③-Connection damage; ④-Overall out-of-plane deflection of lacing; ⑤-Weld cracking)
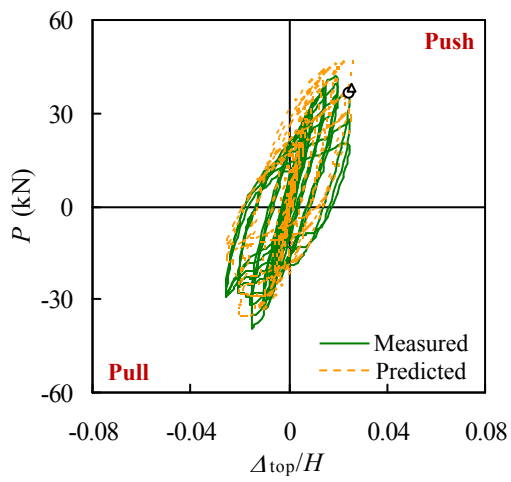
(1) Sa-0.26
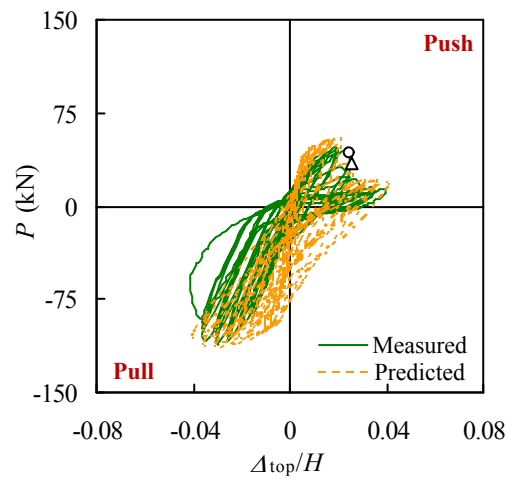
(2) Ca-0.05
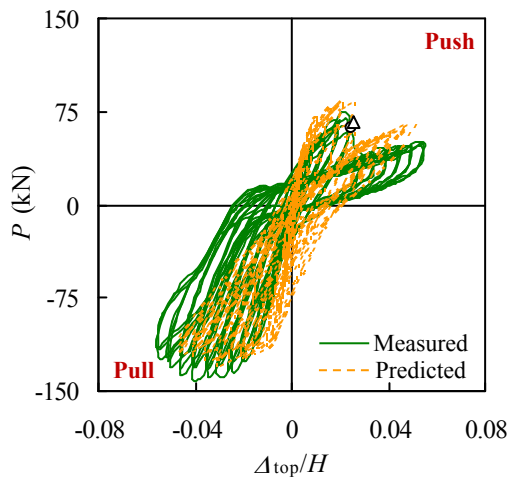
(3) Ca-0.26
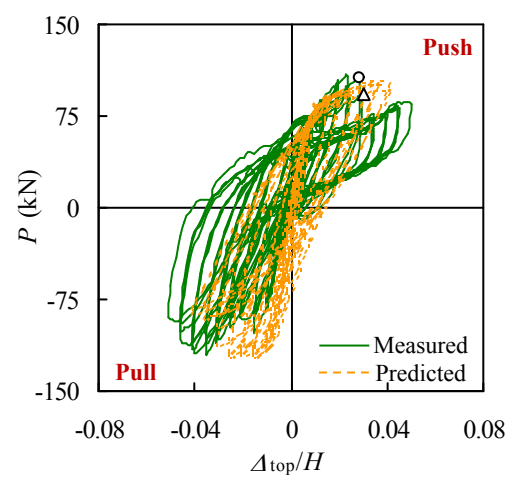
(4) Ca-0.52

(a) $D_s/T_s=51.5$

Fig. 9. (Continued)
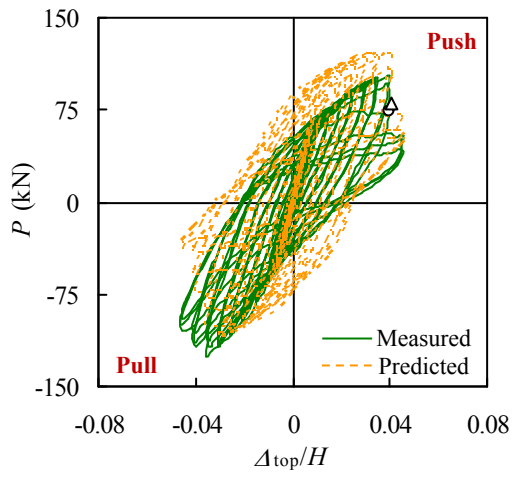
(1) Sb-0.26
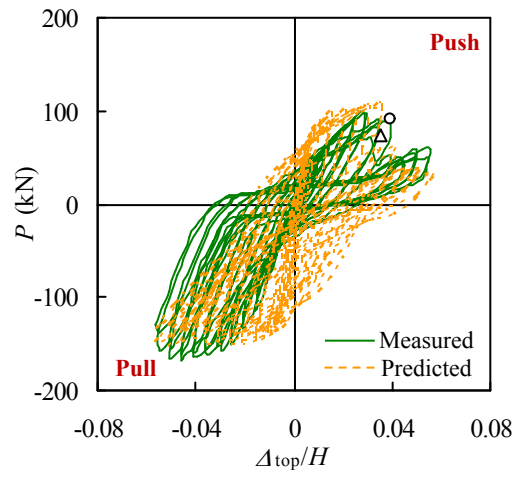
(2) Cb-0.05
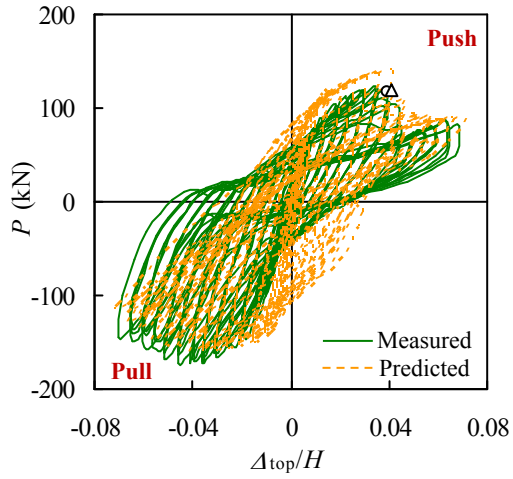
(3) Cb-0.26
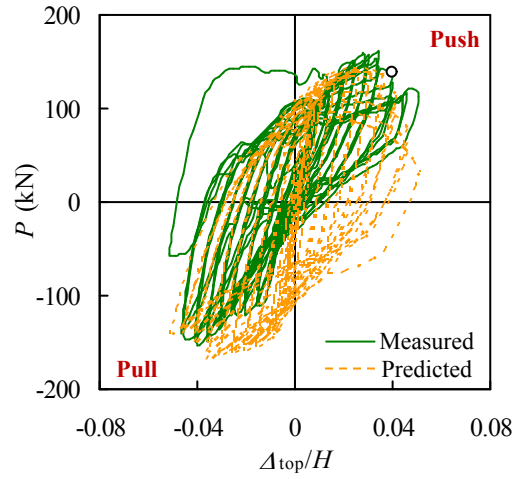
(4) Cb-0.52

(b) $D_s/T_s=24.9$

Fig. 9. $P - \Delta_{top} / H$ hysteretic curve of the specimens.
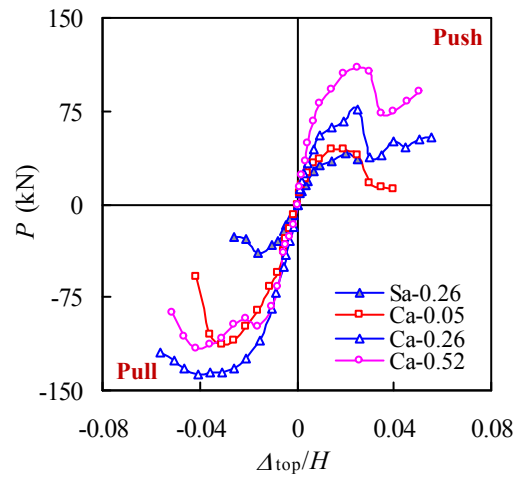
(a) D_s/T_s=51.5
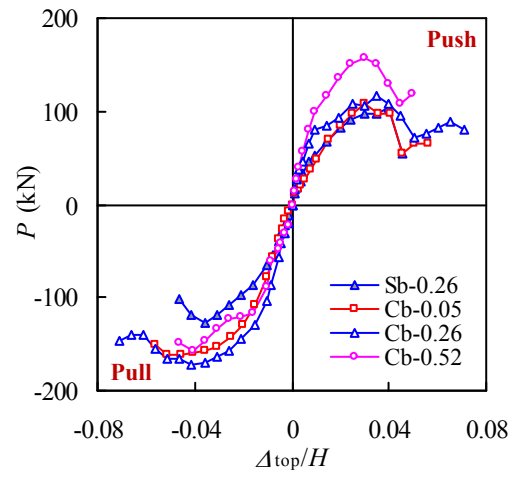
(b) D_s/T_s=24.9

Fig. 10. Comparison of $P - \Delta_{top}/H$ backbone curves.
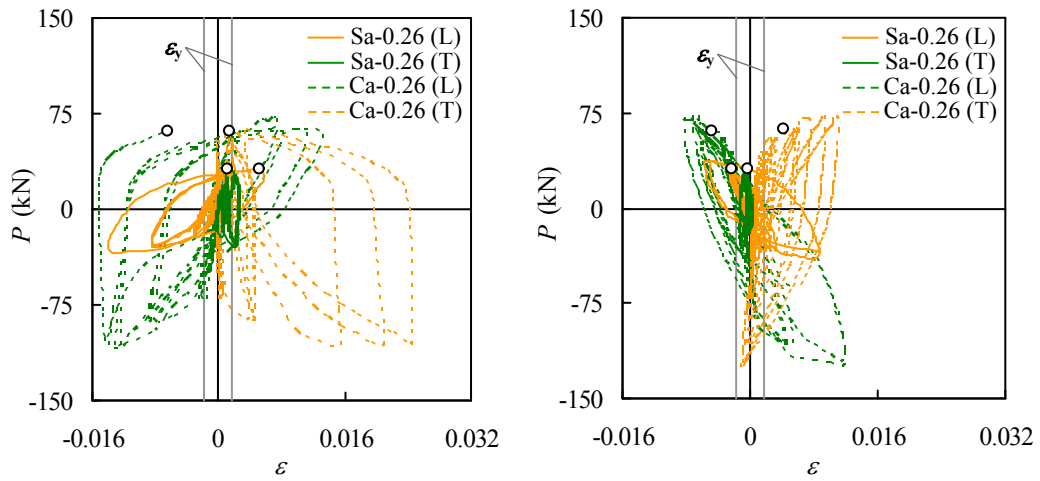
(1) Position A

(2) Position B
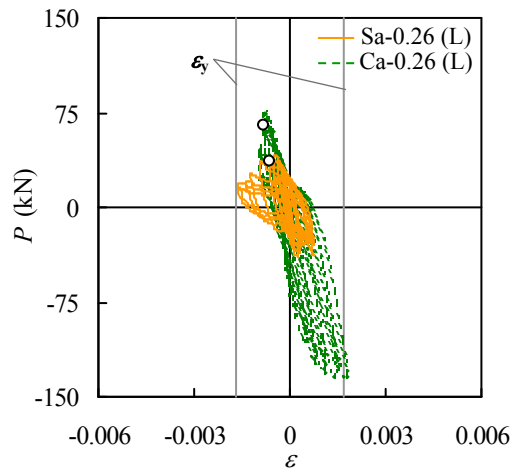
(3) Position E

(a) D_s/T_s=51.5

Fig. 11. (Continued)
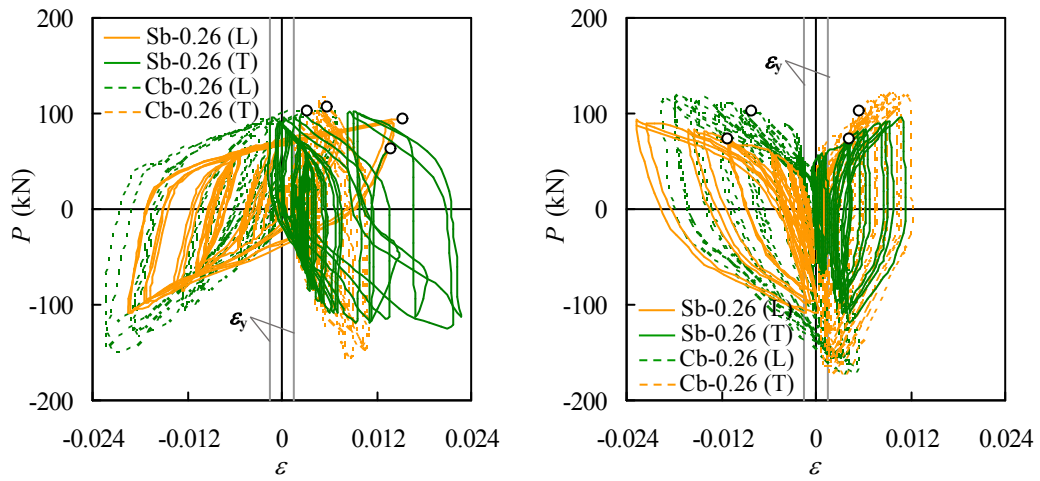
(1) Position A   (2) Position B
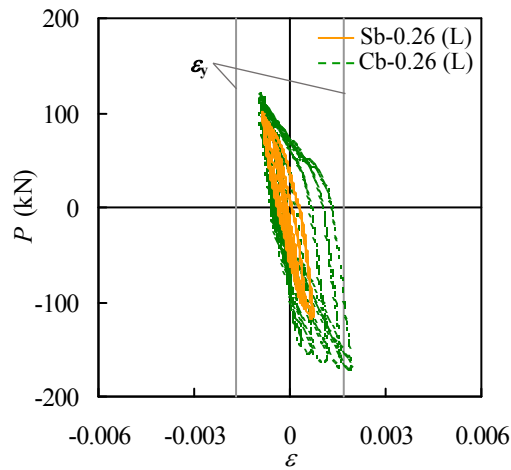
(3) Position E

(b) D_s/T_s=24.9

Fig. 11. Comparison of $P-\varepsilon$ hysteretic curves between CFST latticed specimens and the steel counterparts.
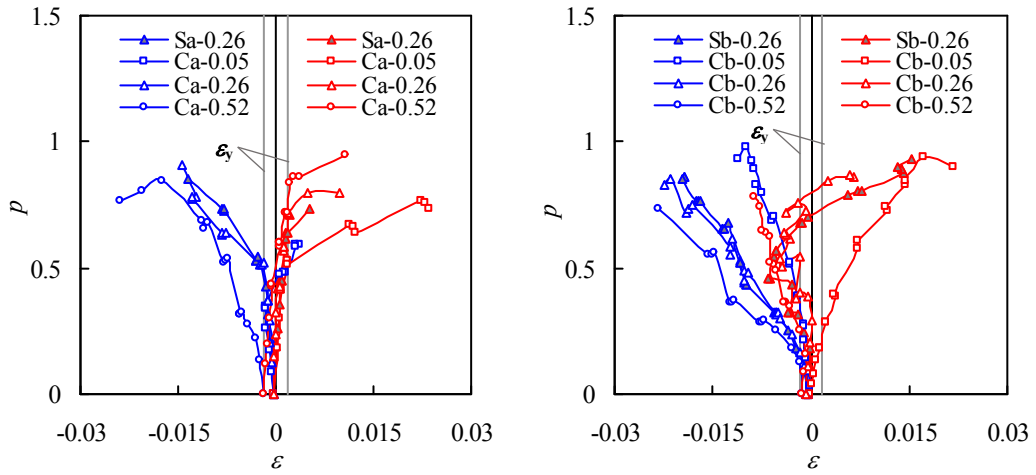
(1) D_s/T_s=51.5　　　　　　　　　(2) D_s/T_s=24.9

(a) Point A
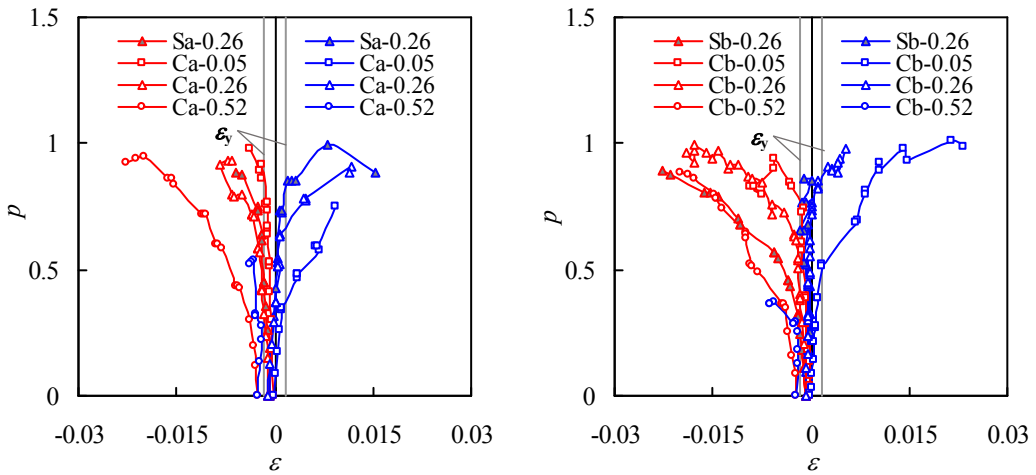
(1) D_s/T_s=51.5　　　　　　　　　(2) D_s/T_s=24.9

(b) Point B
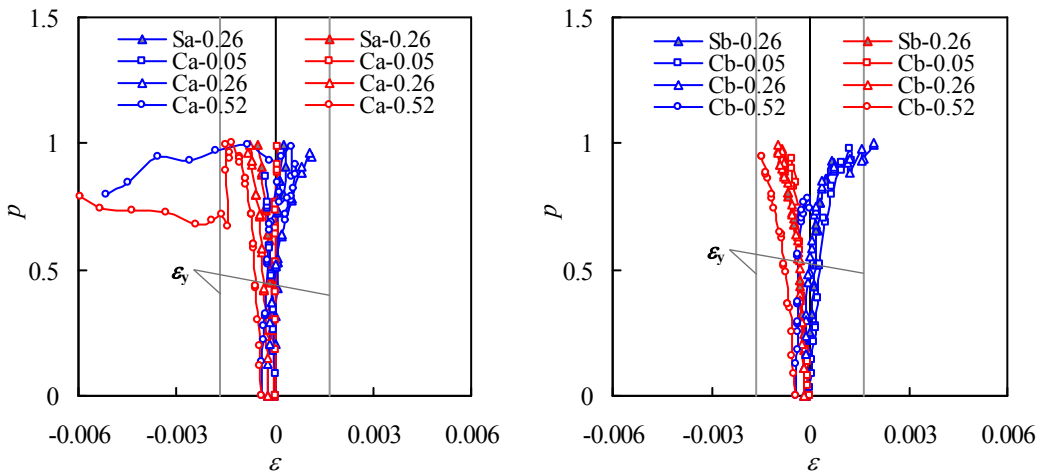
(1) D_s/T_s=51.5　　　　　　　　　(2) D_s/T_s=24.9

(c) Point E

Fig. 12. Effect of parameters on typical $p-\varepsilon$ backbone curves.
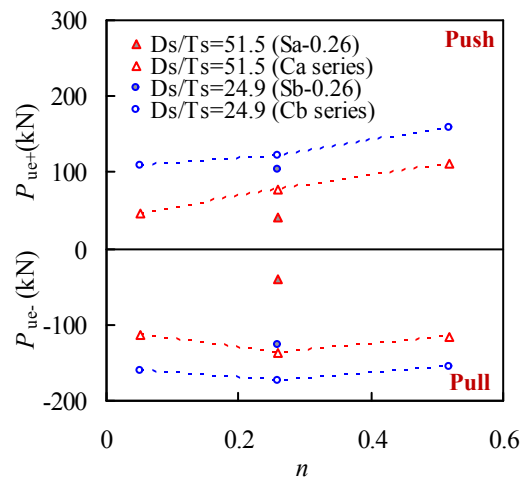
Fig. 13. Effect of parameters on bearing capacities.
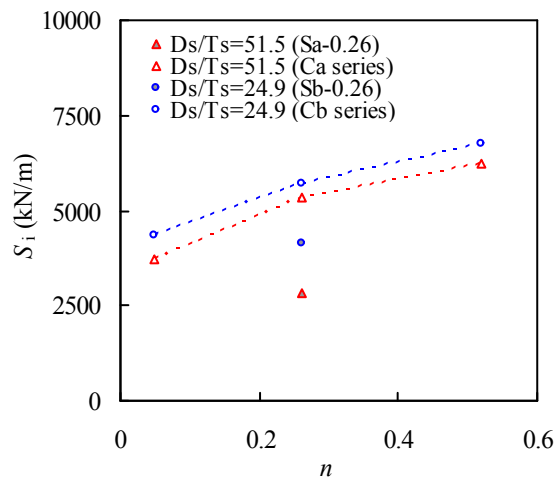
Fig. 14. Variation of S_i.
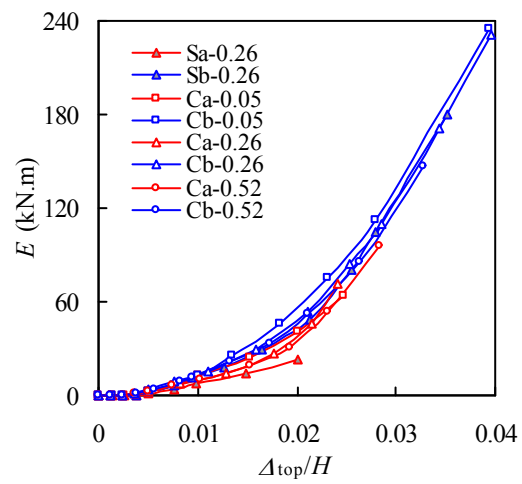
Fig. 15. Comparison of the accumulated energy dissipation (E).
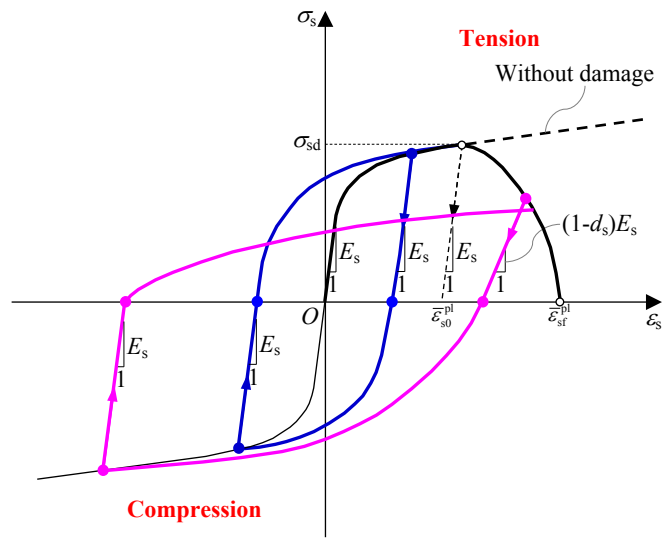
Fig. 16. Cyclic stress (σ_s) versus strain (ε_s) relationship for structural steel with progressive damage degradation.
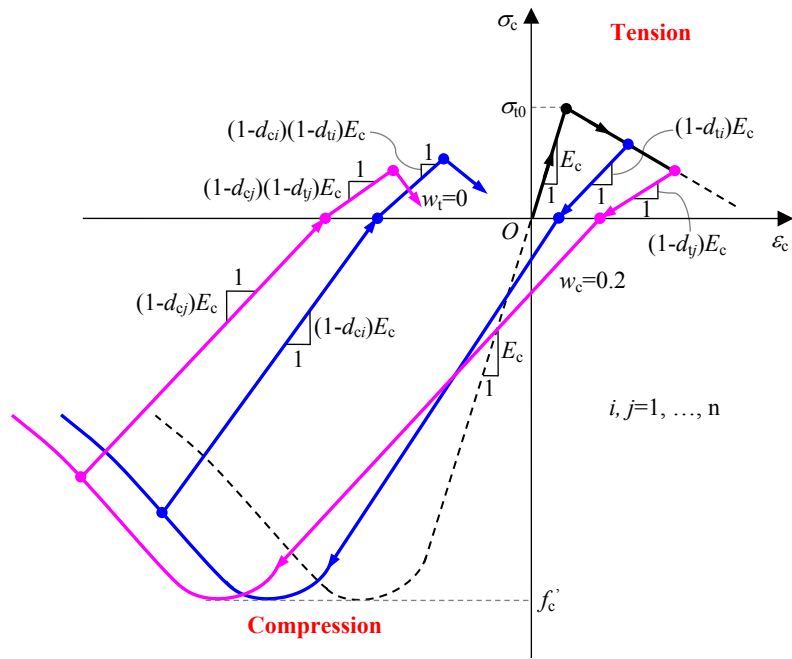
Fig. 17. Cyclic stress (σ_c) versus strain (ε_c) relationship of core concrete in the limbs.
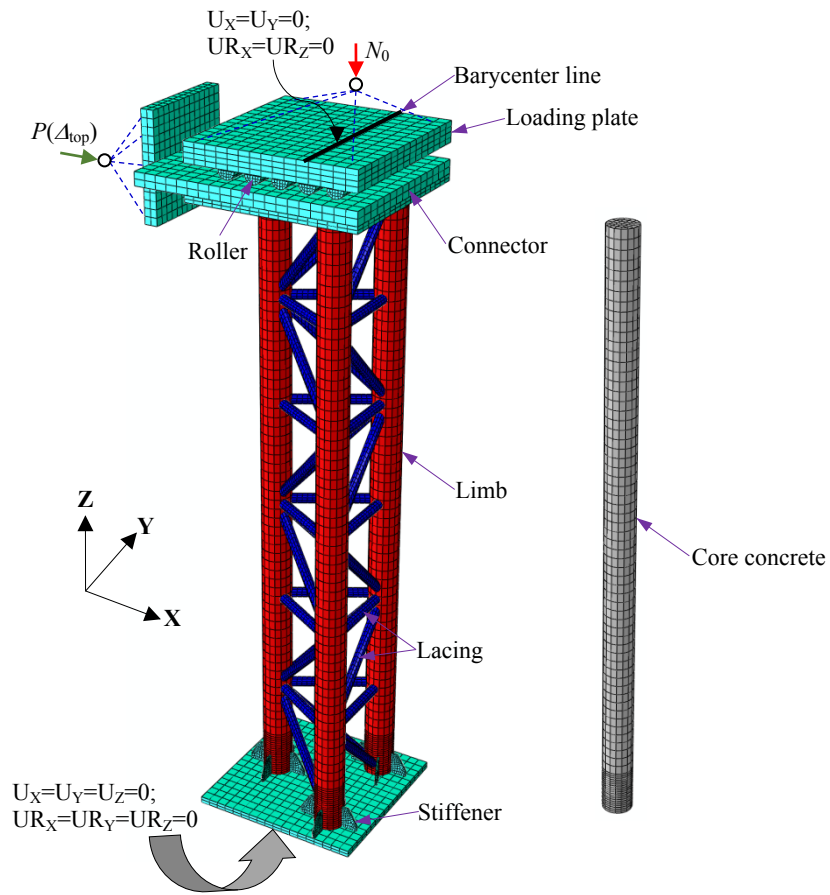
Fig. 18. Meshing and boundary conditions of three-legged CFST columns.
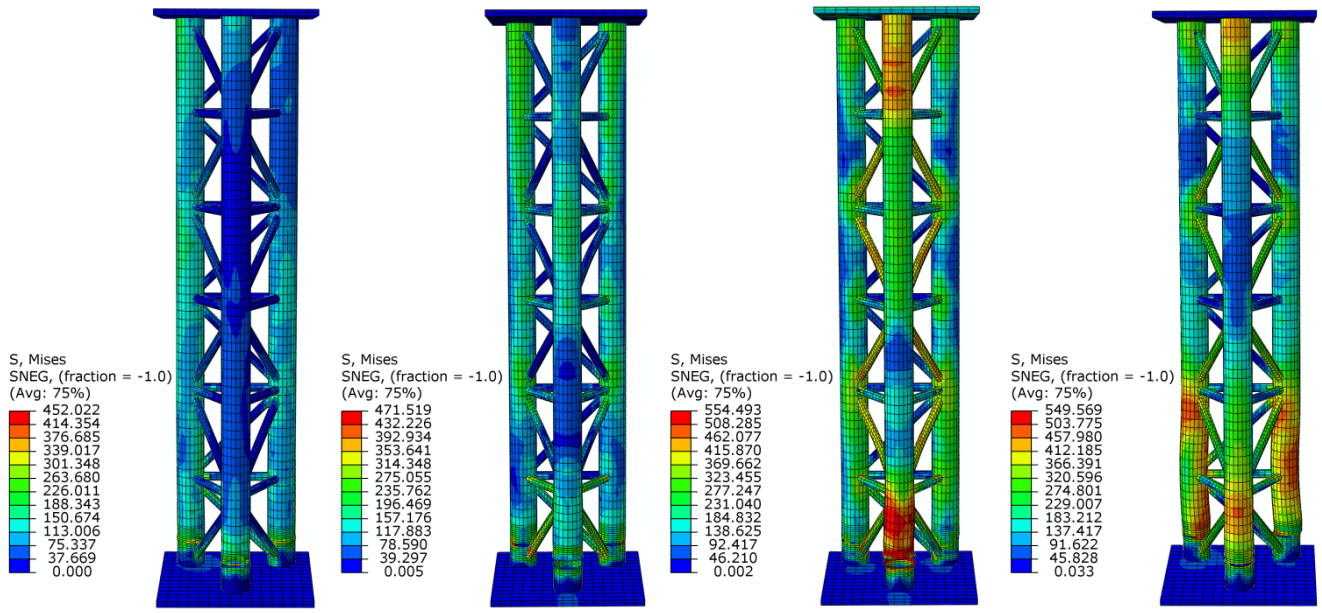
(1) Sa-0.26 (2) Ca-0.05 (3) Ca-0.26 (4) Ca-0.52

(a) D_s/T_s=51.5
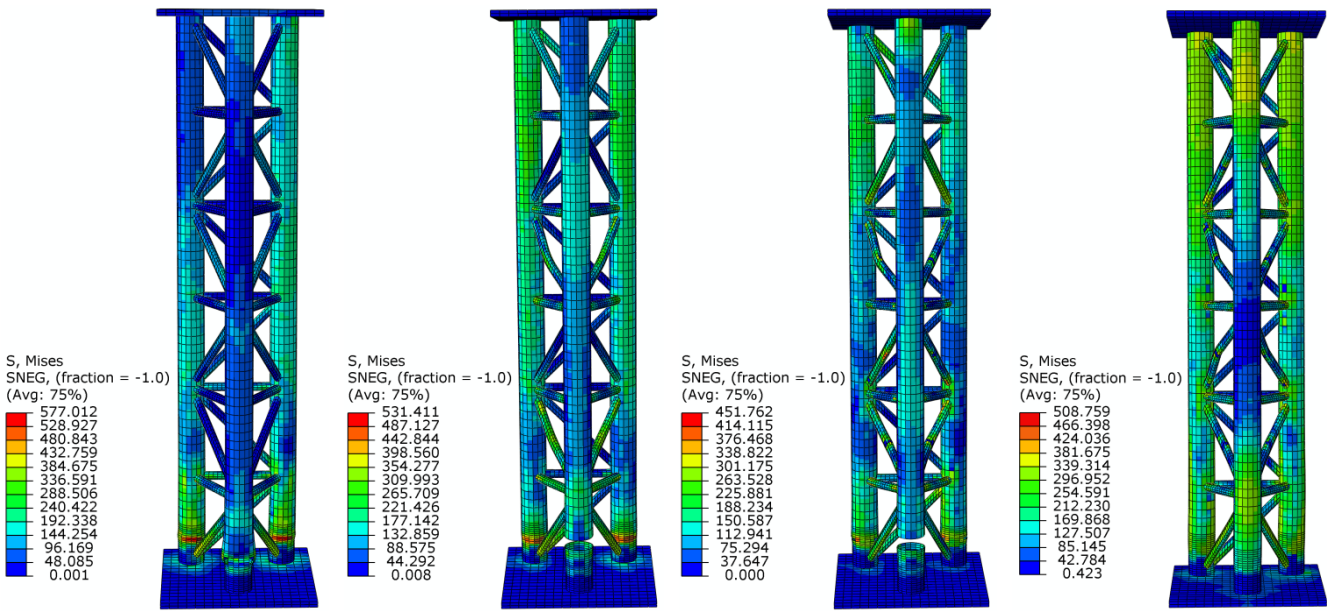
(1) Sb-0.26 (2) Cb-0.05 (3) Cb-0.26 (4) Cb-0.52

(b) D_s/T_s=24.9

Fig. 19. Predicted failure pattern of three-legged CFST specimens using the FEA model.
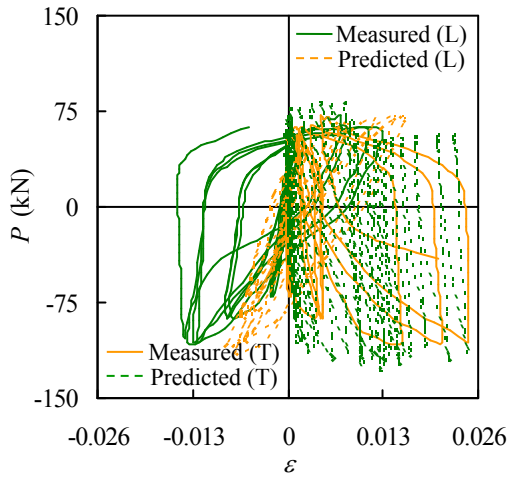
(1) Position A
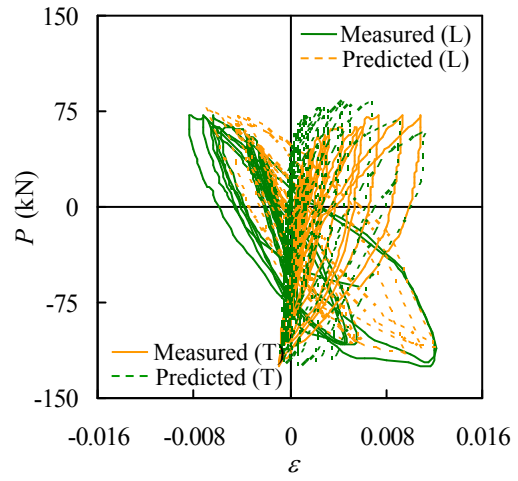
(2) Position B
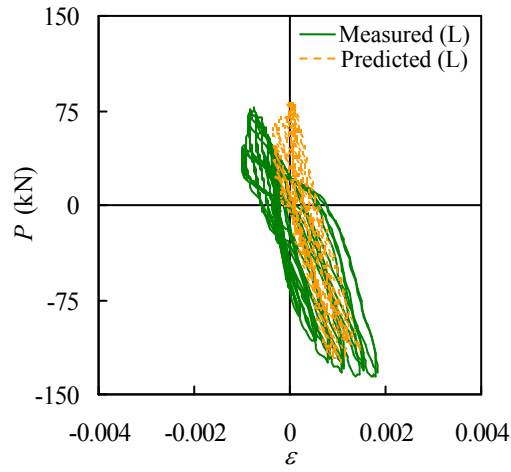
(3) Position E
(a) Ca-0.26
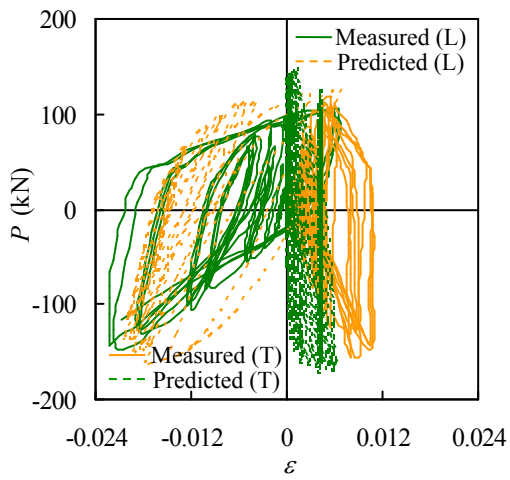
(1) Position A
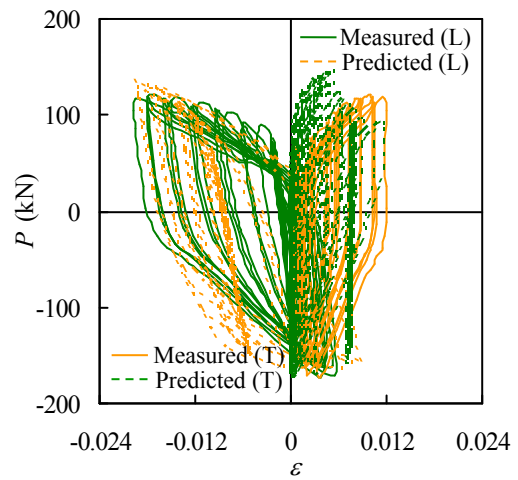
(2) Position B

Fig. 20. (Continued)
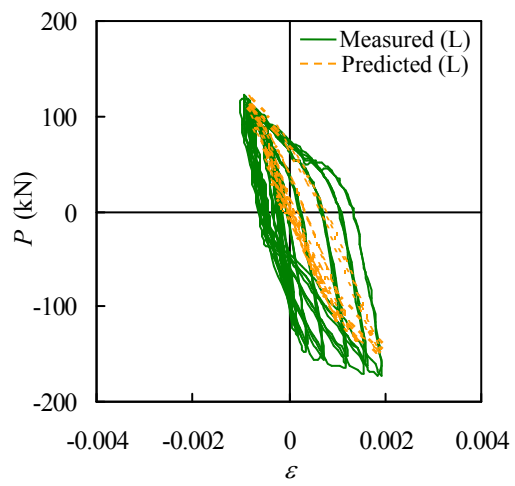
(3) Position E
(b) Cb-0.26

Fig. 20. Typical comparison between the predicted and measured $P-\varepsilon$ hysteretic curves.
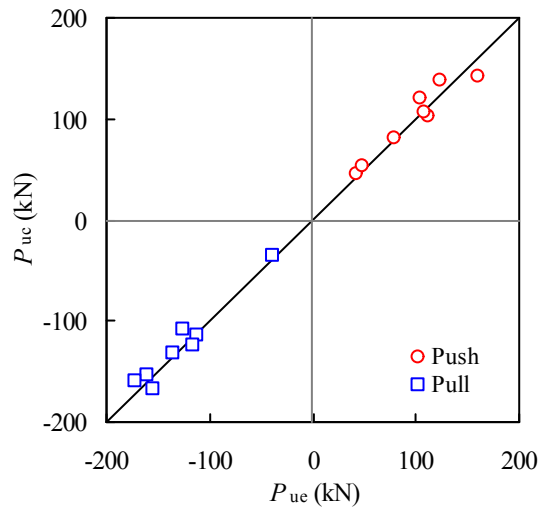
Fig. 21. Comparison between the predicted and measured bearing capacities.
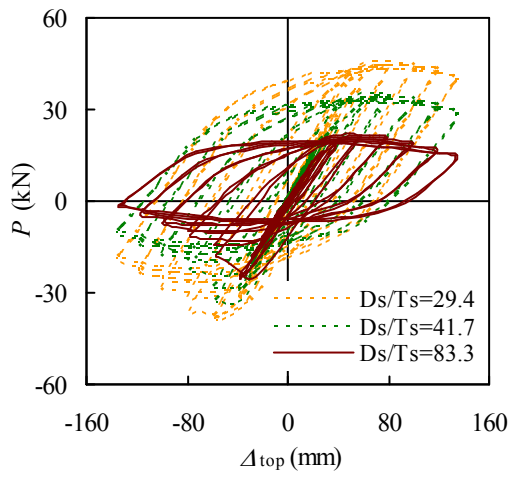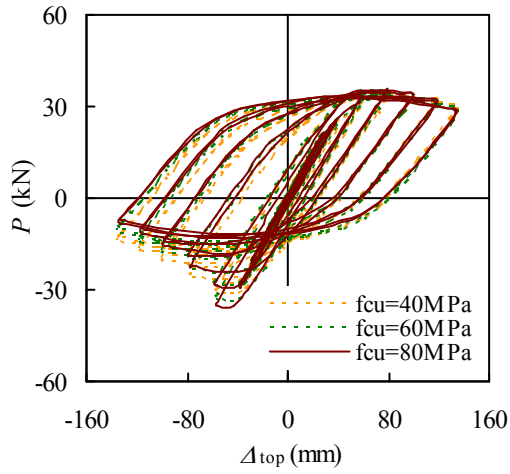
(a) Variation of D_s/T_s
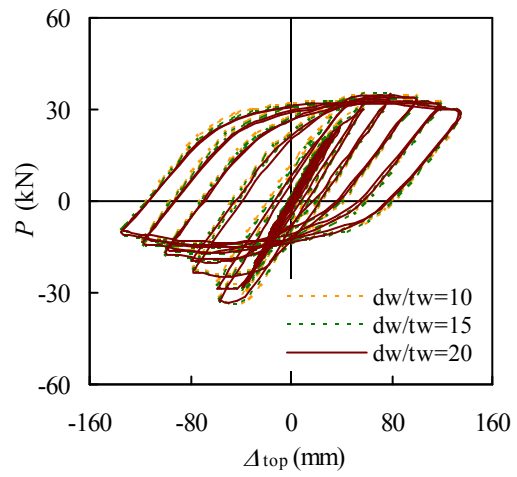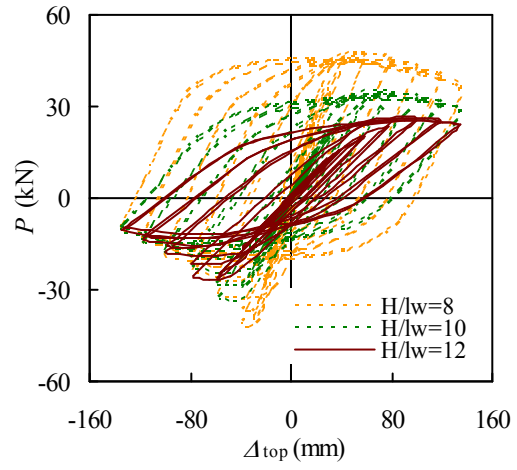
(b) Variation of d_w/t_w
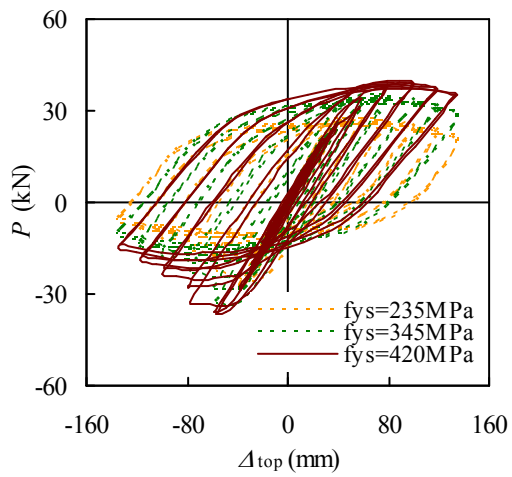
(c) Variation of f_{ys}
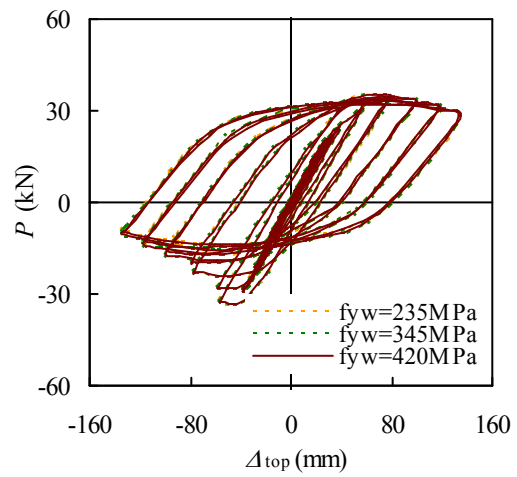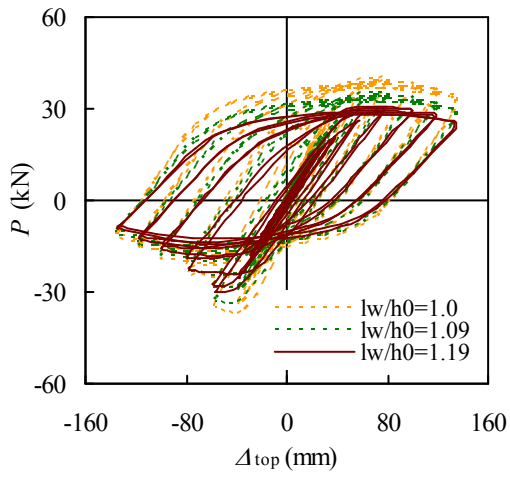
(d) Variation of f_{yw}

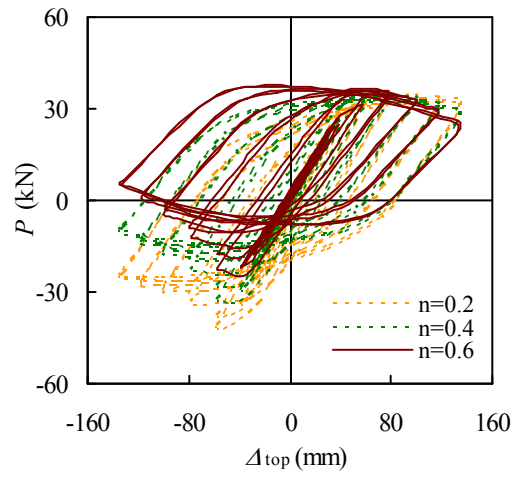**Fig. 22.** (Continued)

57

(e) Variation of f_{cu}

(f) Variation of H/l_w

(g) Variation of l_w/h_0

(h) Variation of n

Fig. 22. Effect of typical parameters on $P-\Delta_{top}$ hysteretic curve of three-legged CFST columns.